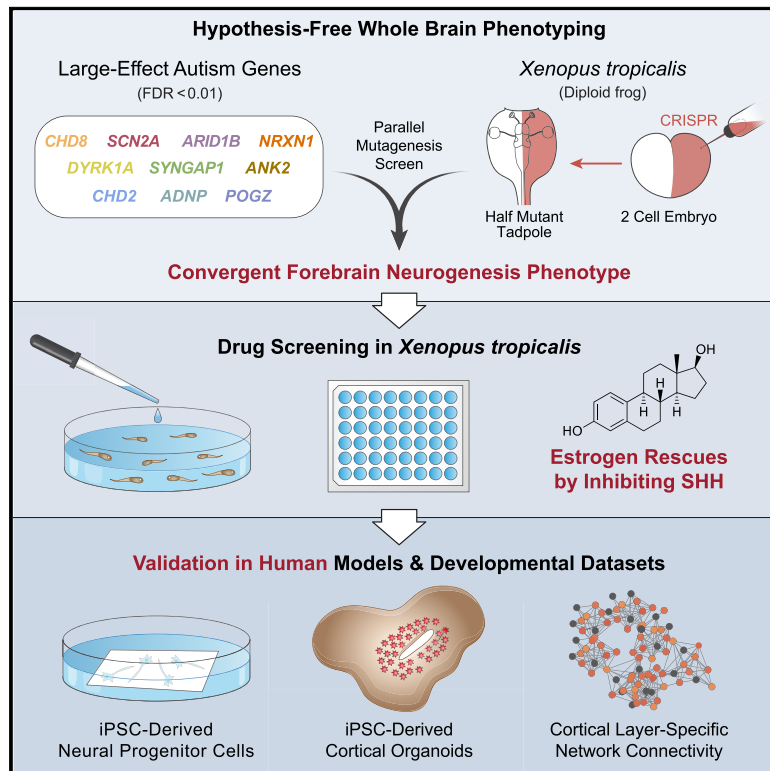


Parallel *in vivo* analysis of large-effect autism genes implicates cortical neurogenesis and estrogen in risk and resilience

Graphical Abstract



Authors

Helen Rankin Willsey,
Cameron R.T. Exner, Yuxiao Xu, ...,
Richard M. Harland, A. Jeremy Willsey,
Matthew W. State

Correspondence

harland@berkeley.edu (R.M.H.),
jeremy.willsey@ucsf.edu (A.J.W.),
matthew.state@ucsf.edu (M.W.S.)

In Brief

Using parallel *in vivo* analyses and systems biological approaches, Willsey et al. implicate cortical neurogenesis as a point of convergent vulnerability in autism spectrum disorders. They identify estrogen as a resilience factor for multiple, disparate autism genes and reveal a conserved role for estrogen in repressing Sonic hedgehog signaling.

Highlights

- *In vivo* analysis of autism genes reveals a convergent vulnerability in neurogenesis
- Systems biological analysis implicates the inner cortical plate and subventricular zone
- Estrogen can mitigate the effects of disparate autism gene mutations
- Estrogen inhibits Sonic hedgehog signaling



Article

Parallel *in vivo* analysis of large-effect autism genes implicates cortical neurogenesis and estrogen in risk and resilience

Helen Rankin Willsey,^{1,2} Cameron R.T. Exner,¹ Yuxiao Xu,^{1,2} Amanda Everitt,^{1,3} Nawei Sun,^{1,3} Belinda Wang,^{1,3} Jeanselle Dea,¹ Galina Schmunk,^{1,4,5} Yefim Zaltsman,^{1,3} Nia Teerikorpi,^{1,3} Albert Kim,^{1,2} Aoife S. Anderson,¹ David Shin,^{1,4,5} Meghan Seyler,^{1,3} Tomasz J. Nowakowski,^{1,4,5} Richard M. Harland,^{2,*} A. Jeremy Willsey,^{1,3,6,*} and Matthew W. State^{1,6,7,8,*}

¹Department of Psychiatry and Behavioral Sciences, UCSF Weill Institute for Neurosciences, University of California, San Francisco, San Francisco, CA 94143, USA

²Department of Molecular and Cell Biology, University of California, Berkeley, Berkeley, CA 94720, USA

³Institute for Neurodegenerative Diseases, UCSF Weill Institute for Neurosciences, University of California, San Francisco, San Francisco, CA 94143, USA

⁴Department of Anatomy, University of California, San Francisco, San Francisco, CA 94143, USA

⁵Eli and Edythe Broad Center for Regeneration Medicine and Stem Cell Research, University of California, San Francisco, San Francisco, CA 94143, USA

⁶Quantitative Biosciences Institute (QBI), University of California, San Francisco, San Francisco, CA 94143, USA

⁷Langley Porter Psychiatric Institute, University of California, San Francisco, San Francisco, CA 94143, USA

⁸Lead contact

*Correspondence: harland@berkeley.edu (R.M.H.), jeremy.willsey@ucsf.edu (A.J.W.), matthew.state@ucsf.edu (M.W.S.)

<https://doi.org/10.1016/j.neuron.2021.01.002>

SUMMARY

Gene Ontology analyses of autism spectrum disorders (ASD) risk genes have repeatedly highlighted synaptic function and transcriptional regulation as key points of convergence. However, these analyses rely on incomplete knowledge of gene function across brain development. Here we leverage *Xenopus tropicalis* to study *in vivo* ten genes with the strongest statistical evidence for association with ASD. All genes are expressed in developing telencephalon at time points mapping to human mid-prenatal development, and mutations lead to an increase in the ratio of neural progenitor cells to maturing neurons, supporting previous *in silico* systems biological findings implicating cortical neurons in ASD vulnerability, but expanding the range of convergent functions to include neurogenesis. Systematic chemical screening identifies that estrogen, via Sonic hedgehog signaling, rescues this convergent phenotype in *Xenopus* and human models of brain development, suggesting a resilience factor that may mitigate a range of ASD genetic risks.

INTRODUCTION

Over the last decade, dozens of genes carrying germline *de novo* likely gene-disrupting mutations have been identified, each contributing large biological effects to autism spectrum disorders (ASD) (Satterstrom et al., 2020; Sanders et al., 2015; Wang et al., 2020). The remarkable degree of locus and biological heterogeneity so far identified has raised understandable concerns of an impenetrably complex biology in which treatments will need to be found for each risk gene or small group of genes. However, from the earliest successful efforts at systematic ASD gene discovery (O’Roak et al., 2012a; Sanders et al., 2012; Neale et al., 2012; Iossifov et al., 2012) systems biological analyses have pointed to a more coherent underlying structure of ASD pathology (Sestan and State, 2018; State and Sestan, 2012; Willsey and State, 2015). For example, Gene

Ontology (GO) analyses of ASD risk genes have repeatedly pointed to a handful of areas of putative biological convergence, most prominently involving the structure and function of the neuronal synapse and the regulation of gene transcription via chromatin modifiers and transcription factors (Ben-David and Shifman, 2013; Satterstrom et al., 2020; De Rubeis et al., 2014; Sanders et al., 2015; Iossifov et al., 2014). Protein-protein interaction analyses have similarly found important points of intersection among the diverse set of risk genes (Chang et al., 2015; Sakai et al., 2011; Li et al., 2015; Ruzzo et al., 2019; O’Roak et al., 2012b), suggesting from the outset that ASD pathology will not resolve to a single or small number of molecular pathways (Sestan and State, 2018). As the characterization of the molecular and cellular landscape of the developing human brain has expanded (Miller et al., 2014; Kang et al., 2011; Tebbenkamp et al., 2014), systems analyses have addressed the question of

spatiotemporal convergence (Willsey and State, 2015). Here, the strongest, replicable findings have pointed to a nexus of vulnerability in human mid-prenatal cortical glutamatergic neurons (Willsey et al., 2013; Parikshak et al., 2013; Xu et al., 2014). These efforts to identify the when and where of ASD pathology have often relied on datasets from postmortem human brain, providing important insights into human biology but also suffering from inherent experimental limitations associated with *ex vivo* computational approaches, including ascertainment bias associated with existing transcriptomic or proteomic datasets, insufficient spatial and temporal resolution, and inability to directly manipulate an intact, developing biological system.

Therefore, we have turned to higher-throughput model organisms and a convergent neuroscience approach with the goals of perturbing many ASD risk genes in parallel and, in a hypothesis-free manner, identifying phenotypes or functions in common as a route to the core biology underlying this condition (Willsey et al., 2018a). Such a convergent approach will minimize the effects of genetic pleiotropy and current biases based on incomplete knowledge of gene function and instead prioritize functions most likely to be relevant to the disorder. Importantly, this convergence could manifest at any level, from physical or genetic interaction networks to higher-order phenotypes, via any number of molecular paths. With this in mind, here we expand the armamentarium for parallelized *in vivo* analyses of ASD risk genes using the model system *Xenopus tropicalis*. We evaluate, in parallel, ten of the highest-confidence ASD risk genes based solely on the strength of their statistical evidence for association with the human condition in search of points of convergence that might begin to differentiate shared ASD-related vulnerabilities from the pleiotropic biology of each gene. *Xenopus* has several key advantages for this purpose, including being relatively high throughput and low cost for an *in vivo* model and providing the opportunity for unilateral mutagenesis by CRISPR-Cas9 injection, allowing the comparison of mutated and control halves of the brain within the same animal throughout vertebrate development (Exner and Willsey, 2020). In addition, its conserved and syntenic diploid genome allows for unambiguous identification of orthologous genes with humans, and a host of studies of human physiology and development have produced important mechanistic insights into congenital heart, kidney, and brain disorders, among others (Exner and Willsey, 2020; Krneta-Stankic et al., 2017; Deniz et al., 2018; Duncan and Khokha, 2016; Garfinkel and Khokha, 2017; Kakebeen and Wills, 2019; Willsey et al., 2018a, 2018b; DeLay et al., 2018). Finally, the approach facilitates not only the investigation of convergent pathology but also an evaluation of *in vivo* resilience mechanisms through small-molecule, chemical, and genetic suppressor screens.

Here we show that all ten ASD-associated genes are expressed during neurogenesis in the *Xenopus* telencephalon. Moreover, in contrast to their many distinct functional roles, disruption in all ten leads to obvious alterations in telencephalic size, a phenotype that is not observed for control brain-expressed genes that have not been shown to carry ASD risk. Detailed analyses of these structural changes, involving increased or decreased brain size, demonstrate that individual disruptions of every gene leads to an increased ratio of neural progenitor cells (NPCs) to differentiating neurons in the devel-

oping telencephalon, pointing to a potential point of convergent vulnerability that expands the long-standing focus on the synapse and transcriptional regulation to include neurogenesis. The developmental timing of this convergent *Xenopus* phenotype maps directly to the human mid-prenatal period, an epoch strongly implicated in ASD risk from co-expression network analyses in humans (Willsey et al., 2013; Parikshak et al., 2013). Moreover, we conduct novel systems biological analyses, leveraging the current list of 102 most strongly associated ASD risk genes, layer-specific gene expression data from the developing human brain, and a comprehensive database of more than 2.7 million molecular interactions. These analyses provide novel evidence for statistically significant convergence of ASD-gene-focused molecular interaction networks in the mid-prenatal inner subventricular zone (SVZ), an area containing proliferating and differentiating NPCs, and provide orthogonal support for ASD risk gene convergence in human cortical neurogenesis. In addition, we search for suppressors and enhancers of the NPC phenotype using hypothesis-free chemical screening approaches and discover that estrogen compounds rescue the convergent phenotype. We pursue this finding and demonstrate an important role for endogenous estrogen signaling in neurogenesis by opposing Sonic hedgehog (SHH) signaling. Finally, we show that both the neurogenesis mutant phenotype and the ability of estrogenic compounds to rescue this convergent dysfunction are conserved in human 2D and 3D *in vitro* models of brain development. These findings expand hypotheses about the convergent pathobiological mechanisms underlying disorder risk beyond the results of *in silico* analyses and single-gene approaches, demonstrate the utility of adding *X. tropicalis* to a range of models supporting ASD systems biological analyses, and identify a novel point of vulnerability in brain development, as well as a potential mechanism of resilience that may be impactful across a range of functionally distinct ASD risk genes. Finally, the finding that estrogen suppresses a convergent ASD-related phenotype in both *Xenopus* and human cell culture prompts intriguing hypotheses regarding the origins of the well-established male predominance of the ASD phenotype.

RESULTS

Top ten ASD risk genes affect telencephalon neurogenesis

We selected the ten genes with the strongest statistical evidence of association with idiopathic autism at the time of initiating this study (Sanders et al., 2015). These genes encode proteins with diverse putative functions spanning historically highlighted GO categories, including gene expression regulation (*CHD8*, *ARID1B*, *CHD2*, *ADNP*, and *POGZ*), neuronal communication (*SCN2A*, *NRXN1*, *SYNGAP1*, and *ANK2*), and a kinase (*DYRK1A*). Since the completion of this study, further sequencing efforts have provided additional evidence that all ten genes are high-confidence ASD (hcASD) risk genes, with seven remaining in the top ten (Satterstrom et al., 2020). All of these genes share the property that likely gene-disrupting/putative loss-of-function coding mutations carry large biological effects.

As a prelude to mutational analyses, we assayed the expression of all ten ASD risk genes by whole-mount RNA *in situ*

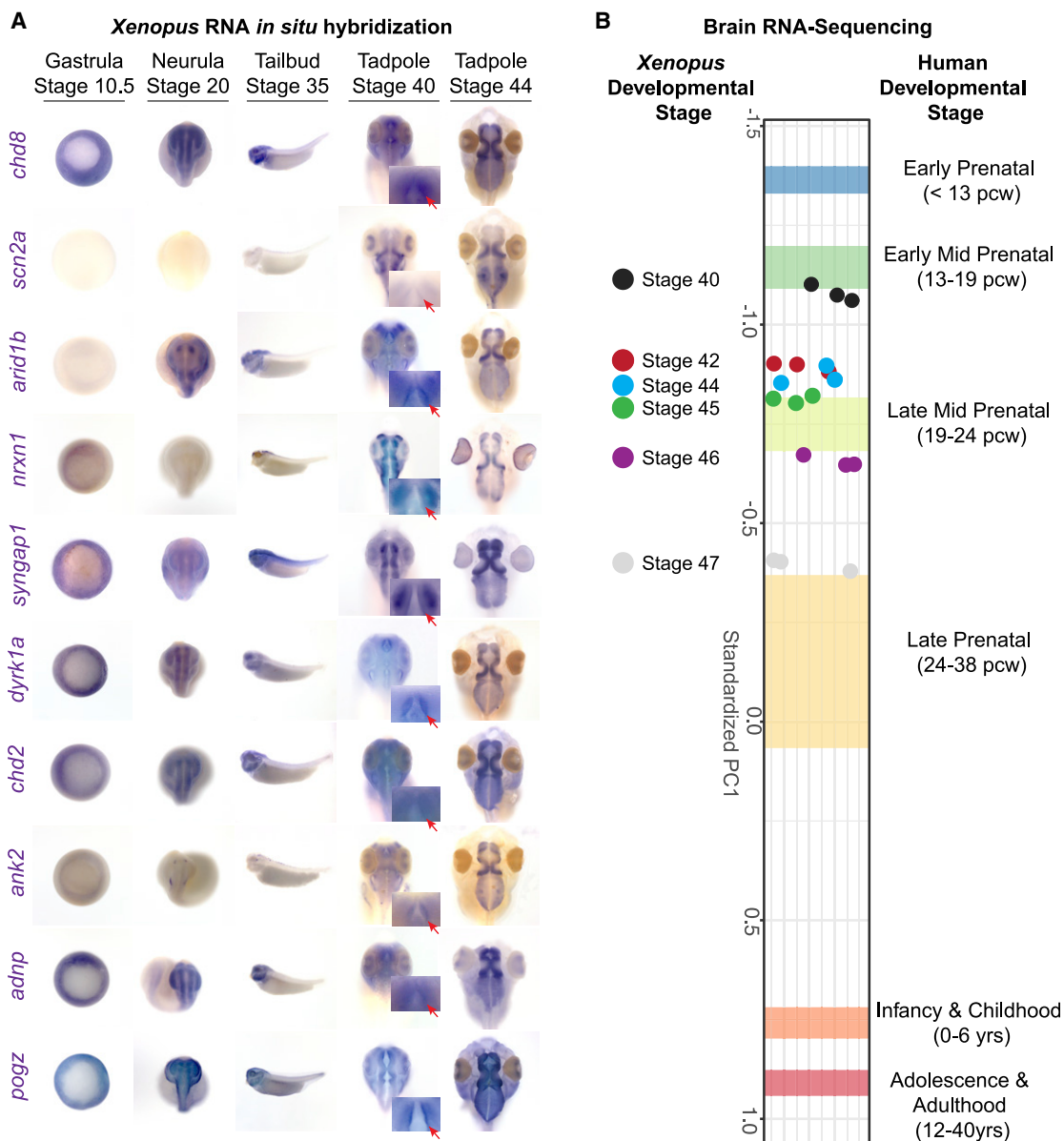


Figure 1. Top ten ASD risk genes are all first expressed during telencephalic neurogenesis

(A) Whole-mount RNA *in situ* hybridization for the top ten ASD risk genes over development in *X. tropicalis*. Note co-expression in stage 40 near the first ventricle (insets with red arrows). See Figure S1 for comparison with marker gene expression patterns.

(B) Mapping *X. tropicalis* brain RNA-seq profiles during tadpole development to human BrainSpan RNA-seq data by principal-component analysis (PCA). Stage 40, when ASD genes are first all expressed in the telencephalon, maps closest to human early mid-prenatal development by plotting principal component (PC) 1, which tracks with developmental age. Bands indicate the mean PC1 value for each human stage plus a 95% confidence interval. *Xenopus* samples are shown as points with three biological replicates. PCW, postconception weeks. See Figures S1C–S1E for full PCA and SEA.

hybridization over development (gastrula Nieuwkoop and Faber [NF] stage 10.5 to free-swimming tadpole NF stage 44) to characterize the distribution of expression and to determine whether there are points of spatiotemporal gene expression overlap, a putative indicator of convergence (Figures 1A, S1A, and S1B; Table S1). We first detected expression of all ten ASD risk genes in the developing brain at stage 40 (early tadpole), with most showing particularly strong expression in the telencephalon

near the first ventricle, where NPCs expressing *pax6* and *pcna* reside (Figures 1A, S1A, and S1B). Expression of all ten genes continued through stage 44, when most genes were expressed more widely throughout the brain (Figure 1A).

We next set out to assess the temporal correspondence of ASD risk gene expression between *Xenopus* and human brain development to anchor our observations to human neurodevelopment. We generated RNA sequencing (RNA-seq) data from

tadpole whole-brain dissections spanning NF stages 40–47. As observed in the RNA *in situ* hybridizations, all ten ASD genes are expressed in all stages. Notably, 94 of 102 recently reported ASD genes (Satterstrom et al., 2020) show expression at one or more stages during this time, representing highly statistically significant enrichment ($p = 1.14E-23$, hypergeometric test). We next compared the tadpole brain transcriptome from stages 40–47 to the human BrainSpan developmental transcriptome using principal-component analysis (Kang et al., 2011). These *Xenopus* stages show a clear pattern of maturation and map most closely with human samples from early mid-prenatal to late prenatal stages (Figures 1B, S1C, and S1D). We observed similar mapping with an orthogonal method, specific expression analysis (SEA) (Xu et al., 2014) (Figure S1E; Table S2). Therefore, all ten ASD risk genes are co-expressed in the telencephalon at time points mapping to human mid-prenatal brain development, consistent with previous analyses that identified convergence of ASD risk gene expression during this epoch in humans (Willsey et al., 2013; Parikshak et al., 2013).

To determine whether these apparently functionally divergent genes may underlie a shared point of developmental vulnerability, we modeled loss-of-function variants in all ten genes using CRISPR-Cas9 mutagenesis in *X. tropicalis* (Figures 2A and S2; Table S1). We grew animals to free-swimming tadpoles for whom large-scale, whole-brain imaging is practical (NF stage 46) and evaluated for gross anatomical/developmental differences between mutant and wild-type cells. *Xenopus* has the distinctive advantage of being able to generate unilaterally mutant animals, divided by the midline, and allow matched internal controls (Figure 2A) (Exner and Willsey, 2020). Thus, we compared mutant to wild-type halves within individual tadpoles with the goal of identifying shared phenotypes across the diverse set of risk genes. We observed a significant change in telencephalon size for all mutants (Figures 2B–2H, S2, and S3; $p < 0.05$ by Mann-Whitney rank-sum tests; increase for *scn2a*, *arid1b*, *nrxn1*, and *ank2*; decrease for *chd8*, *syngap1*, *dyrk1a*, *chd2*, *adnp*, and *pozg*). We did not observe a change in telencephalic size for six independent controls, including two non-ASD-associated yet brain-expressed genes *phrf1* and *itpr3*, both of which have been identified in congenital heart disease based on *de novo* variation (Jin et al., 2017) (Figures 2B, 2H, S2, and S3). Combining all mutants, telencephalon size variance was significantly changed following ASD risk gene mutation ($p < 0.0001$ by a Brown-Forsythe test), whereas variance in mesencephalon, diencephalon, and rhombencephalon sizes was not (Figures S3A and S3B). We used a well-characterized morpholino (*dyrk1a* MO) (Blackburn et al., 2019) and a pharmacological inhibitor (harmine) (Göckler et al., 2009) to validate our findings for the gene *dyrk1a* (Figures S3C–S3F), and injection of human *DYRK1A* (*hDYRK1A-GFP*) rescued the *Xenopus dyrk1a* CRISPR phenotype (Figures 2F, 2G, and 2I).

Given the particularly strong expression of ASD risk genes co-localizing with NPCs lining the ventricle in the telencephalon, we reasoned that the observed changes in brain size might reflect shared alterations in neurogenesis. Consequently, we assessed whether the number of NPCs expressing PCNA (proliferating cell nuclear antigen) was altered in ASD risk gene mutants versus controls. In general, mutants with larger telencephalons had

more NPCs, whereas mutants with smaller telencephalons had fewer NPCs (Figures 3A–3C). Next, we assessed NPC development by measuring the ratio of NPCs to differentiated neurons by quantifying PCNA versus vGlut1 (vesicular glutamate transporter 1) staining. For all ten ASD risk genes, the ratio of NPCs to differentiated neurons was significantly increased in mutants (Figure 3D), implying defects in NPC proliferation, survival, and/or differentiation. We again validated the *dyrk1a* mutant phenotype with harmine, as well as two well-characterized pharmacological inhibitors (TG003 and proINDY) (Ogawa et al., 2010), and observed a similar decrease in telencephalon size and a similar relative increase in NPCs for all three compounds (Figures S4A–S4G).

To determine whether the observation of a convergent phenotype in frog was recapitulated in human cells, we tested whether decreased expression of ASD risk genes in human induced pluripotent stem cell (iPSC)-derived NPCs alters the relative proportion of proliferative cells (Ki67⁺). We generated CRISPR interference (CRISPRi) lines in human NPCs targeting five of the selected ASD risk genes representing diverse annotated cellular functions (*NRXN1*, *DYRK1A*, *CHD2*, *ADNP*, or *POGZ*) and compared the proportion of Ki67⁺ cells with paired nontargeting CRISPRi control lines. Consistent with the observations in *Xenopus*, CRISPRi perturbation of *NRXN1*, *DYRK1A*, *CHD2*, or *ADNP* led to a statistically significant increase in the relative proportion of Ki67⁺ proliferative cells, and for *POGZ*, it led to a trend in this direction that did not reach statistical significance (Figure 3E). Altogether, these results suggest that disruption of these ASD risk genes affects NPC biology, which manifests as a relative increase in NPCs compared with mature neurons, irrespective of gross telencephalon size in frog, and that similar alterations in NPCs are present in *Xenopus in vivo* and in human neuronal cell culture in response to ASD mutations in functionally diverse risk genes.

Overall, these data point to a convergent phenotype in *Xenopus* emerging from mutations in ten apparently functionally divergent ASD risk genes chosen solely on their statistical evidence for association with the human diagnosis. These genes are all expressed in forebrain, alter brain size upon disruption, and show a shared phenotype of increased NPCs in both frog and human cellular models. In addition, the expression of these ASD risk genes in *Xenopus* corresponds to the epoch of human brain development implicated in ASD risk by human co-expression analyses (Willsey et al., 2013; Parikshak et al., 2013).

ASD risk gene convergence in human cortical NPCs

Previous systems biological analyses of human transcriptome data identified mid-prenatal cortical neurons as points of convergent ASD vulnerability, based on the finding of an over-representation of associated risk genes in co-expression networks corresponding to this developmental epoch and anatomical region (Willsey et al., 2013; Parikshak et al., 2013). Independent analyses have highlighted both deep-layer (Willsey et al., 2013) and upper-layer (Parikshak et al., 2013) cortical glutamatergic neurons as susceptible cell types. However, these initial studies were conducted early in the process of systematic ASD gene discovery when the number of genes meeting accepted statistical thresholds for association with the human phenotype was

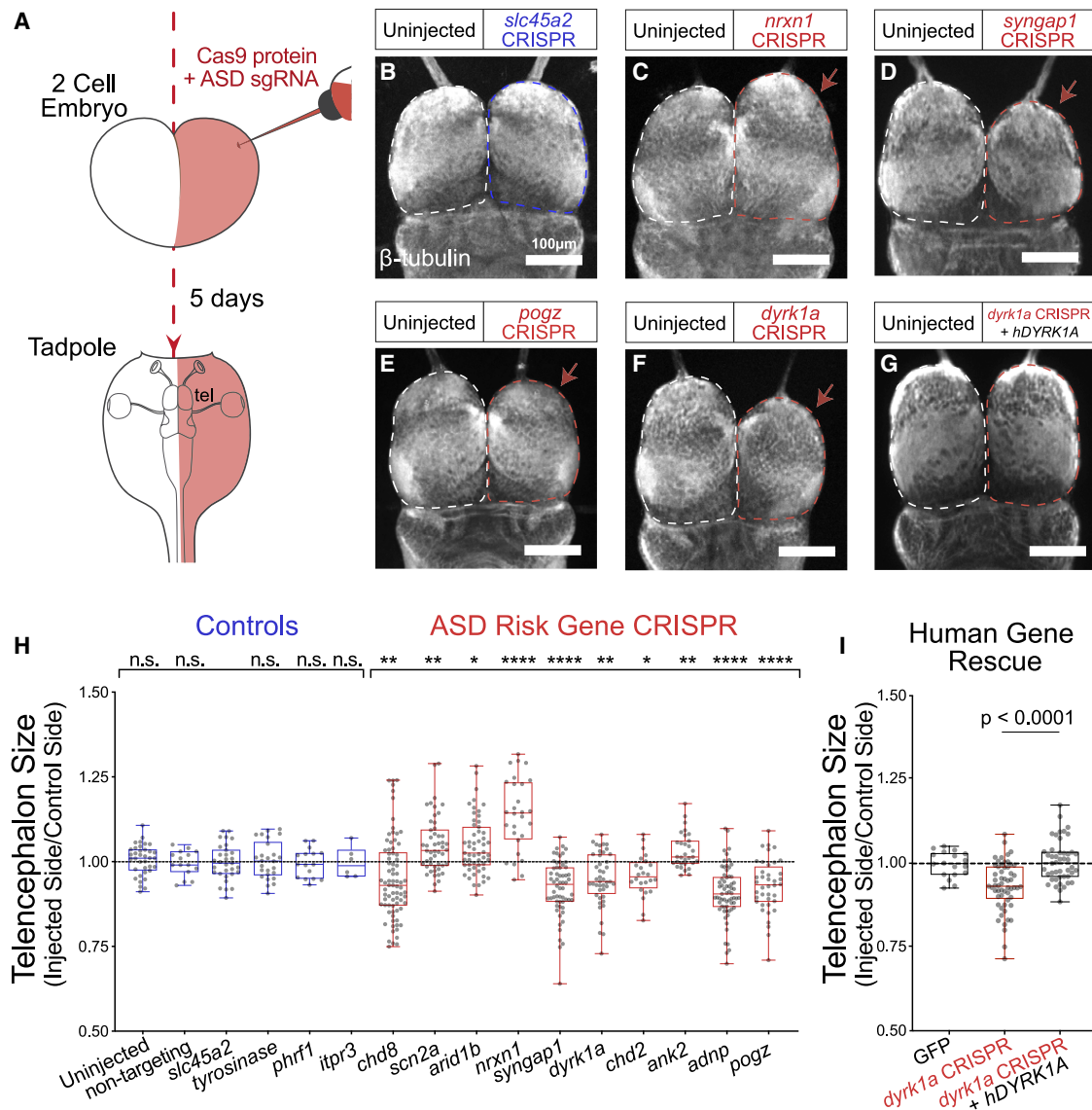


Figure 2. Top ten ASD risk genes affect telencephalon size

(A) Unilateral mutants are made by injecting Cas9 protein, a single-guide RNA (sgRNA) for an ASD risk gene, and dye (red) into one cell of two-cell stage *X. tropicalis* embryos. tel, telencephalon.

(B) Control CRISPR (right side) targeting pigmentation gene *slc45a2* has a symmetric brain (β-tubulin stain). Telencephalon region for each half is outlined by a dotted line.

(C–F) Mutating *nrxn1* (C) increases telencephalon size, whereas mutating *syngap1* (D), *pogz* (E), or *dyrk1a* (F) decreases it.

(G) Human *DYRK1A* plasmid injection rescues *dyrk1a* CRISPR.

(H) Telencephalon size quantification by targeted gene. Controls (blue) and ASD risk gene CRISPRs (red). Measurements are normalized by the within-animal control side. p values are from nonparametric Mann-Whitney rank-sum tests, compared with *slc45a2* CRISPR. n.s., not significant, indicates p > 0.05. *p < 0.05, **p < 0.01, ***p < 0.001, and ****p < 0.0001. See Figure S2 for mutational efficiencies and control CRISPR images and Figure S3 for other brain region measurements.

(I) Human gene rescue quantification, nonparametric Mann-Whitney test.

relatively small. Consequently, we elected to study the latest set of 102 high-confidence genes to determine whether we could bring greater spatiotemporal resolution to the human transcriptome analyses and to clarify whether these findings are consistent with a role for neurogenesis as a convergent ASD risk phenotype (Figure 4A).

To conduct this analysis, we created an ASD-centric molecular interaction network by combining the 102 hcASD risk genes (Satterstrom et al., 2020) with PCNet (Parsimonious Composite Network), a comprehensive database of more than 2.7 million molecular interactions among 19,781 human genes (Huang et al., 2018). Specifically, we trimmed the genes in PCNet to

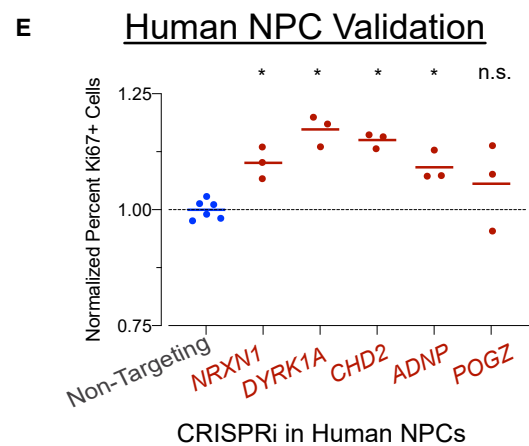
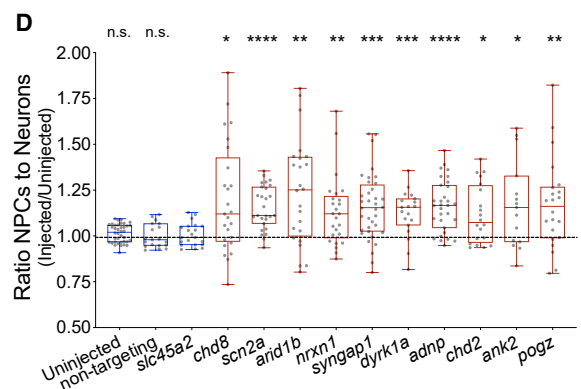
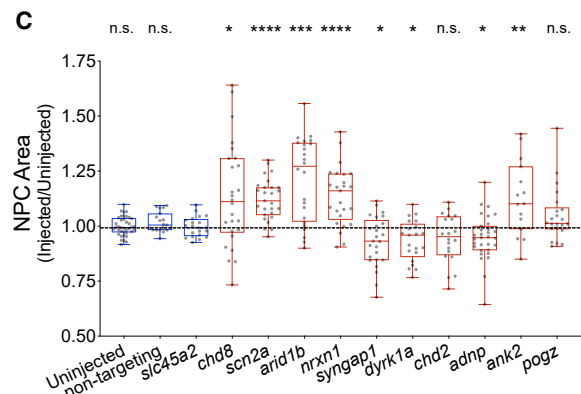
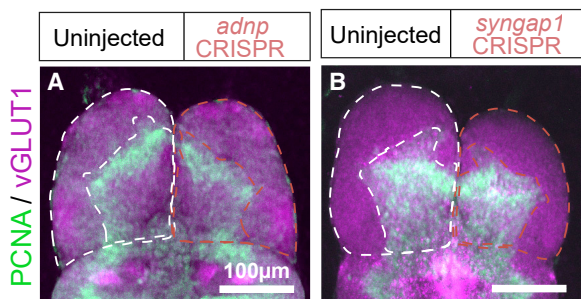


Figure 3. Top ten ASD risk genes affect NPC maturation

(A and B) Mutating *adnp* (A) or *syngap1* (B) reduces ventricle size (green). Telencephalon and ventricle are outlined by a dotted line.

(C) NPC area quantification from PCNA staining by the targeted gene (blue are controls, and red are ASD risk genes). Measurements are normalized by the within-animal control side.

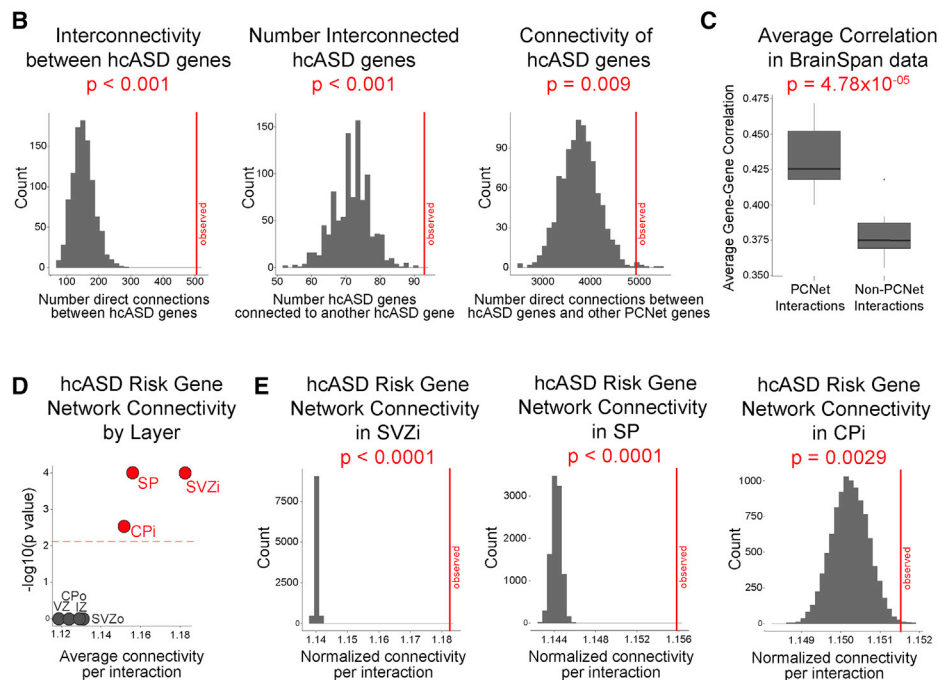
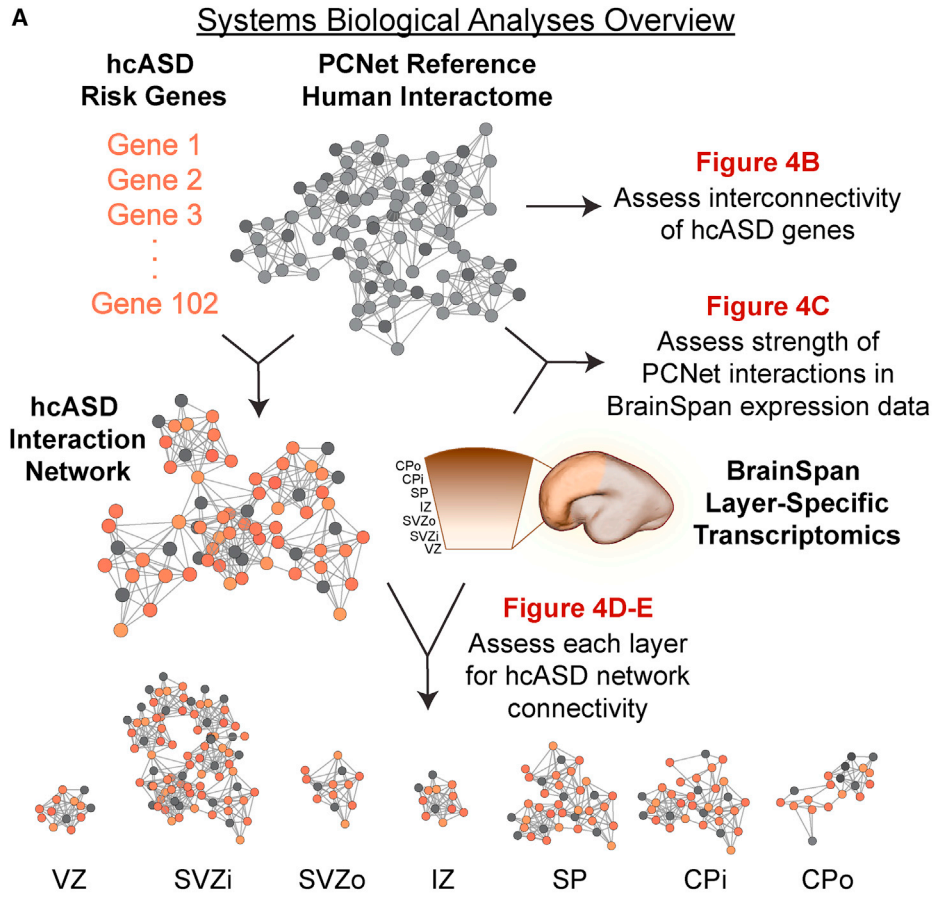
(D) NPC to differentiated neuron quantification by gene.

(E) CRISPRi against ASD risk genes in human NPCs causes an increase in the proportion of Ki67⁺ proliferative NPCs. p values are from nonparametric Mann-Whitney rank-sum tests, in which n.s. (not significant) indicates $p > 0.05$. * $p < 0.05$, ** $p < 0.01$, *** $p < 0.001$, and **** $p < 0.0001$.

hcASD genes and their direct interactors, maintaining all cataloged edges between these genes (i.e., connections between hcASD genes, between hcASD and direct interactor genes, and between direct interactor genes). We then leveraged BrainSpan layer-specific microarray gene expression data from laser microdissected (LMD) prenatal human brains (Miller et al., 2014) to create layer-specific molecular interaction networks and assessed their connectivity, with the hypothesis that significantly increased connectivity versus null expectation would identify ASD risk gene convergence.

More specifically, we first checked whether the hcASD genes are highly connected in PCNet, as has been observed previously in protein-protein interaction data (O’Roak et al., 2012b; Sanders et al., 2015). 98 of 102 hcASD genes are represented in PCNet, including all ten ASD genes studied here, and these genes are indeed more interconnected than expected by chance (Figure 4B). Next, based on the hypothesis that interacting genes will have higher gene expression correlation than noninteracting genes, we compared the average correlation of genes connected in PCNet versus unconnected genes. Consistent with this hypothesis, interacting genes tend to be more highly correlated (Spearman’s rank correlation coefficient) across all BrainSpan microarray expression data (Figure 4C). Altogether, these results suggest that PCNet captures relationships between hcASD genes that are recapitulated in gene co-expression analysis and therefore that it is meaningful to combine PCNet with layer-specific gene expression data to generate layer-specific molecular interaction networks.

We next generated an ASD-centric interaction network by trimming PCNet to interactions involving either hcASD genes or direct interactors of hcASD genes. We then created layer-specific interaction networks by trimming to expressed genes in each layer and estimating the strength of each known molecular interaction as the gene expression correlation in that layer. The BrainSpan prenatal LMD microarray dataset spans four donors, corresponding to postconception week (PCW) 15, PCW16, PCW20, and PCW21. We focused on the frontal cortex data from PCW15 (male) and PCW16 (female) donors only, because these time points correspond best to *Xenopus* stage 40 (Figures 1B and S1C–S1E), when co-expression of all ten ASD genes is observed, and match the period and brain region of the strongest ASD risk gene convergence in the human developing brain (Willsey et al., 2013). This dataset also encompasses 9 layers of the frontal cortex: subplial granular zone (SG), marginal zone (MZ), outer and inner cortical plate (CPo, CPi), subplate (SP), intermediate zone (IZ), outer and inner subventricular zone (SVZo, SVZi), and ventricular zone (VZ) (referring to developmental layers, not



(legend on next page)

layers 1–6 of mature neocortex (Miller et al., 2014). SG and MZ had only a few samples across PCW15–PCW16 (0 SG samples and 3 MZ samples); therefore, we excluded these layers from our analyses and focused on the remaining 7 layers, spanning VZ to CPo (each layer had at least 7 independent samples). For each layer, we estimated the strength of ASD gene convergence based on the connectivity of the layer-specific interaction network. Specifically, we estimated this as the sum of the absolute value of correlation coefficients for all network gene pairs present in that layer. We observed that the SVZi is the most highly connected layer, whether looking at total normalized connectivity (data not shown) or normalized connectivity per interaction (Figure 4D). Because of differences in layer-specific network sizes due to differences in the number of genes expressed in each layer, we focused on the average connectivity per interaction (a value >1 indicates that the network interactions tend to be more highly correlated than the average correlation coefficient in that layer).

We next assessed the significance of the observed layer-specific hcASD network connectivities using a permutation test with 10,000 iterations and determined that SVZi and SP have higher connectivity than expected by chance ($p < 0.0001$), as does CPi ($p = 0.0029$) (Figures 4D and 4E). Therefore, this analysis supports previous findings implicating CPi as a nexus of ASD risk gene convergence (Willsey et al., 2013) and newly identifies SVZi and SP as additional points of convergence enriched for ASD risk genes; SVZi has the strongest signal of all layers. This is notable given that intermediate progenitor cells within the SVZi are highly proliferative and neurogenic (Ortega et al., 2018; Zecevic et al., 2005; Kriegstein et al., 2006; Martínez-Cerdeño et al., 2006), providing an independent line of evidence that early neurogenesis may be a key nexus of ASD risk (Packer, 2016). Within the SVZi, the ten ASD genes targeted in this study do not have significantly different connectivity compared with the remaining hcASD genes ($p = 0.55$, Mann-Whitney rank-sum test), suggesting that these genes are not outliers with respect to the broader group of 102 hcASD genes.

Oncology drug screen identifies estrogen as a suppressor of the ASD phenotype

We next reasoned that we could leverage the relative ease of chemical screening in *Xenopus* to pinpoint potential molecular mechanisms underlying the convergent NPC phenotype and/or to identify general resilience factors to multiple ASD genetic

risks. Such a finding may provide a path forward to therapeutics development, even in the absence of detailed gene-by-gene mechanistic insights. We selected the National Cancer Institute Approved Oncology Drugs Set VIII, a library of 133 U.S. Food and Drug Administration (FDA)-approved oncology drugs, because these compounds typically target proliferative cells. Given the logistical challenges of screening this many compounds against CRISPR-injected mutants, we first focused on elaborating the biological mechanisms of the NPC proliferation phenotype using *dyrk1a*, the only top ten ASD risk gene with a well-characterized chemical inhibitor (harmine), and used this compound to conduct a primary screen for interactors. We tested all compounds from the library at 10 μM , in combination with 1.25 μM harmine, and measured the ratio of NPCs to differentiated neurons. As expected, DYRK1A inhibition (red dashed line) alone increased this ratio compared with DMSO control (blue dashed line) (Figure 5A). Of the 133 compounds, 8 suppressed the phenotype (6%), 9 enhanced the phenotype (7%), 32 were lethal (24%), and 84 had no effect (63%) (Figure 5A; Table S3). Of the 17 compounds that altered the phenotype, 3 were involved in estrogen signaling (Table S3). A pathway agonist (estramustine) suppressed the phenotype, whereas inhibitors of estrogen signaling (fulvestrant and raloxifene) enhanced it. Furthermore, anastrozole, an aromatase inhibitor, and therefore a negative regulator of estrogen signaling, narrowly missed our cutoff for enhancement (ratio = 1.45, cutoff = 1.47) (Table S3). This result was particularly striking given our prior findings from an unbiased chemical screen in zebrafish that estrogens rescue a behavioral phenotype caused by a well-established recessive autism risk gene, contactin-associated protein 2 (*CNTNAP2*) (Hoffman et al., 2016). We next tested whether the most prevalent, endogenous form of estrogen, 17- β -estradiol, could rescue the effect of DYRK1A inhibition, which it did (Figures 5B–5E), even restoring the spatial arrangement of NPCs.

Estrogen signaling is required for telencephalic neurogenesis and inhibits SHH signaling

These data raised the question of whether endogenous estrogen signaling contributes to neurogenesis during telencephalon development. It has been previously shown that the estrogen receptors are present and expressed in *Xenopus* (Takase and Iguuchi, 2007; Wu et al., 2003). To look specifically at the developing nervous system, we conducted *in situ* RNA hybridization

Figure 4. Expression and functional convergence of ASD risk genes in human NPCs

(A) Overview of analysis. We integrate the top 102 hcASD risk genes (Satterstrom et al., 2020) with the PCNet human interactome reference database (Huang et al., 2018) and BrainSpan layer-specific prenatal human frontal neocortex microarray gene expression data (Miller et al., 2014) to construct layer-specific hcASD interaction networks. We then identify the brain layer or layers with the strongest convergence of hcASD molecular interactions.

(B) hcASD genes are more connected than expected by chance in PCNet, as measured by the number of direct PCNet interactions among hcASD genes ($p < 0.001$), total number of hcASD genes that are connected to at least one other hcASD gene ($p < 0.001$), and number of interactions with hcASD genes and any other gene in PCNet ($p = 0.009$). The red line indicates the observed value, and the gray histogram shows the null distribution of 1,000 permutations.

(C) PCNet interactions have higher expression correlation in BrainSpan layer-specific expression data than non-PCNet interactions ($p = 4.78 \times 10^{-5}$). 7 BrainSpan layers were assessed (VZ, SVZi, SVZo, IZ, SP, CPi, and CPo), and the p value was obtained by a paired sample t test.

(D) SVZi-specific hcASD interaction network has the highest average connectivity per interaction.

(E) SVZi has significantly higher hcASD interaction network connectivity than expected by chance ($p < 0.0001$), as do SP ($p < 0.0001$), and CPi ($p = 0.0029$). The red line indicates the observed connectivity, and the gray histogram shows the null distribution from 10,000 permutations.

hcASD, high-confidence ASD; VZ, ventricular zone; SVZi, inner subventricular zone; SVZo, outer subventricular zone; IZ, intermediate zone; SP, subplate; CPi, inner cortical plate; CPo, outer cortical plate.

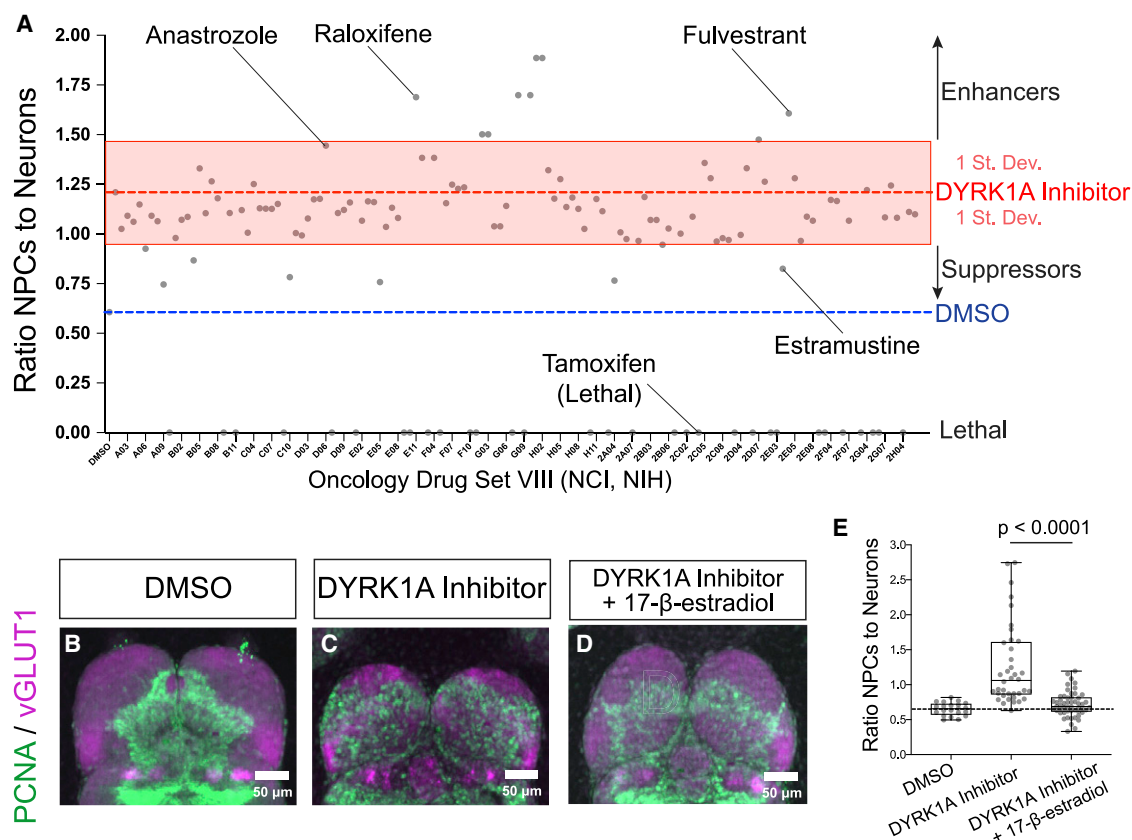


Figure 5. Drug screen identifies estrogen as a suppressor of the convergent ASD phenotype

(A) DYRK1A inhibitor alone (1.25 μ M harmine) increases the ratio of NPCs to neurons (red dashed line) compared with control (DMSO, blue dashed line). See Figure S4 for harmine validation. Each point is the mean ratio following treatment with a 10 μ M NCI Approved Oncology Drugs Set VIII drug and 1.25 μ M harmine. Several estrogen pathway drugs modified the phenotype (change greater than one standard deviation [SD]), including estramustine (pro-estrogen), fulvestrant (estrogen receptor modulator), and raloxifene (aromatase inhibitor).

(B–D) 10 μ M 17- β -estradiol suppresses the convergent ASD phenotype generated by 1.25 μ M harmine treatment.

(E) Quantification of (B)–(D). The *p* value is from a Mann-Whitney test.

experiments and observed expression of core estrogen pathway members in the developing *Xenopus* brain at stage 40, with expression of estrogen receptor α (*ER α /esr1*), estrogen receptor β (*ER β /esr2*), and aromatase (*cyp19a1*, the enzyme required for the synthesis of 17- β -estradiol from testosterone) localizing near the first ventricle (Figures 6A–6C, red arrows). This raised the possibility for local estrogen production and signaling. This location also overlaps the expression patterns of the ASD genes. Next, we made unilateral CRISPR mutants for these components, and in all cases, we observed changes in telencephalon size, phenocopying ASD risk gene mutants (Figures 6D–6G; all $p < 0.05$ by Mann-Whitney test). We validated *ER β* and *cyp19a1* CRISPRs with MOs (Figure 6G; $p < 0.0001$ by Mann-Whitney test). Altogether, our results suggest that local estrogen signaling is required during telencephalic neurogenesis and disruption of this pathway mimics the convergent ASD phenotype.

To generate hypotheses about the molecular pathways downstream of estrogen signaling in the developing brain, we conducted RNA-seq and identified differentially expressed (DEX) genes in *Xenopus* whole brain following 17- β -estradiol treatment

(Table S4). SHH signaling targets (e.g., *dlx1*, *dlx2*, *nkx2.1*, and *lhx6*) (Ericson et al., 1995; Chiang et al., 1996; Ohkubo et al., 2002; Fuccillo et al., 2004; Anderson et al., 1997; Shimamura and Rubenstein, 1997) were strongly repressed, suggesting that estrogen may inhibit SHH signaling (Figure 7A). Consistently, estrogen-treated brains had midline defects (Figures 7B and 7C), a classic SHH mutant phenotype (Chiang et al., 1996). Next, we treated animals with cyclopamine, a specific SHH signaling inhibitor (Chen et al., 2002), conducted RNA-seq, and identified DEX genes. Consistent with the known role of cyclopamine in regulating SHH signaling, we observed repression of downstream SHH targets (Figure 7A; Table S4). Of the 320 DEX genes following estrogen treatment, 235 (73%) are DEX in the same direction with a fold change ≥ 2 following cyclopamine treatment, a concordance that is statistically striking (Figure 7A; Table S4; $p = 8.83 \times 10^{-213}$ by hypergeometric test) and suggests functional overlap. Similar to estrogen, cyclopamine decreased the ratio of NPCs to differentiated neurons and caused midline defects (Figures 7B–7E; $p < 0.001$ by Mann-Whitney test). Therefore, we predicted that SHH inhibition should also suppress the increased NPC-to-neuron ratio observed

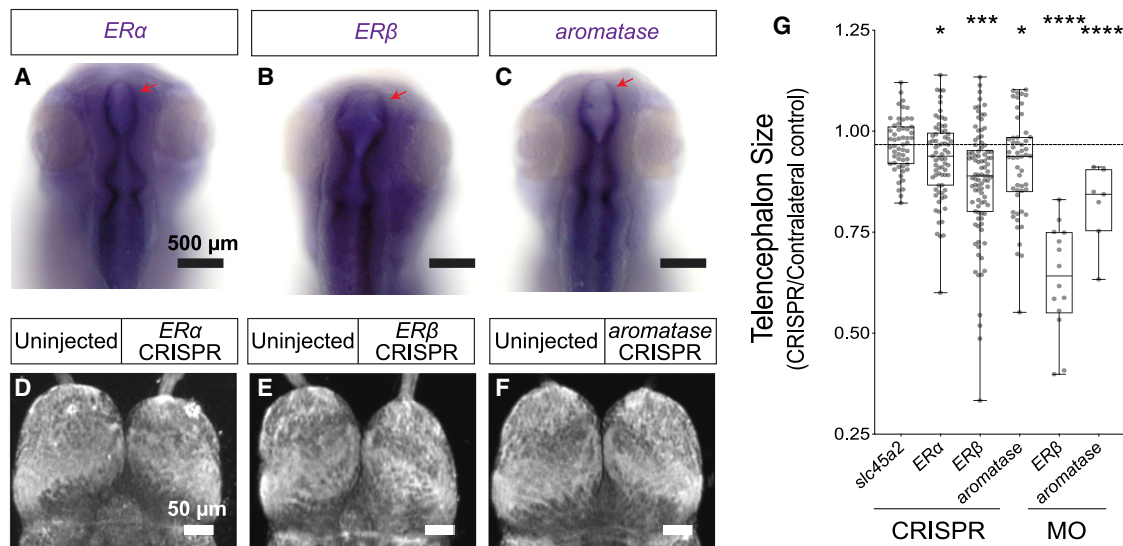


Figure 6. Estrogen signaling is required for telencephalon development

(A–C) Whole-mount RNA *in situ* hybridization on stage 40 *X. tropicalis* embryos highlights expression of estrogen receptor α (*ER α /esr1*, A), estrogen receptor β (*ER β /esr2*, B), and aromatase (*cyp19a1*, C) in the telencephalon (red arrows). (D–G) Unilateral loss of estrogen pathway components reduces telencephalon size autonomously (β -tubulin stain). (G) Quantification of telencephalon size by condition (normalized by contralateral control). p values are from nonparametric Mann-Whitney rank-sum tests, in which n.s., not significant, indicates $p > 0.05$. * $p < 0.05$, ** $p < 0.01$, *** $p < 0.001$, and **** $p < 0.0001$.

following ASD risk gene inhibition. Cyclopamine treatment significantly ameliorated Dyrk1a inhibition ($p < 0.001$), moving the ratio of NPCs to differentiated neurons closer to control levels (Figures S4H–S4K). Finally, we tested whether these pathways are opposed and found that 17- β -estradiol treatment rescued ectopic SHH activation by Smoothed agonist (SAG) (Lewis and Krieg, 2014) (Figures S4L–S4O; $p < 0.001$ by Mann-Whitney test). Moreover, similar to cyclopamine, 17- β -estradiol treatment caused a marked reduction in expression of the SHH target gene *patched1* (*ptch1*), whereas inhibiting estrogen production with aromatase inhibitor I increased *ptch1* expression (Figures 7F–7I). Altogether, these results suggest that estrogen signaling inhibits SHH signaling and that this opposition may be important for regulating neurogenesis.

Importantly, we previously showed that Dyrk1a functions during neurogenesis in this context by regulating cell-cycle progression, potentially via its role in regulating microtubule dynamics at the mitotic spindle (Willsey et al., 2020). This raises the salient point that the molecular mechanism of rescue may be distinct from the original perturbation but function in the same overall process. A more general resilience factor that would intersect multiple ASD risk genes would not necessarily share the same molecular mechanisms as individual genes.

Estrogen confers resilience to multiple ASD genetic risks in human *in vitro* models

Next, we tested the interaction of estrogen with the convergent ASD phenotype in human *in vitro* model systems. We assayed whether treatment with 17- β -estradiol could rescue the relative increase in proliferative Ki67⁺ NPCs derived from human CRISPRi cell lines repressing three genes of apparently disparate cellular function (*DYRK1A*, *NRXN1*, or *ADNP*). Indeed, in

all three ASD risk gene CRISPRi lines, treatment with estrogen significantly moved the proportion of Ki67⁺ cells closer to that of nontargeting control lines (Figure 8A). We validated this interaction in a 3D model of human brain development. We treated human cortical organoids with DMSO, 17- β -estradiol, harmine, or both and assayed proliferation by Ki67 staining. Consistent with *Xenopus* and human NPCs, 17- β -estradiol treatment decreased the proportion of proliferating cells, DYRK1A inhibition by harmine increased it, and treatment together moved it closer to control levels (Figures 8B–8E). Thus, in both *Xenopus* and human model systems, activating estrogen signaling reduces the number of proliferative progenitor cells and modulates the convergent phenotype resulting from ASD risk gene disruption. We next tested the endogenous relevance of this finding by inhibiting estrogen signaling with a stable CRISPRi human dorsal forebrain NPC line repressing *ER β /ESR2* and assaying whether these cells showed NPC-relevant defects during neural differentiation. We observed a significant increase in NPC markers such as *EMX2*, *VIM*, and *HES1* after exposure to conditions promoting differentiation to excitatory neurons (Figure S5; Table S5), suggesting disruptions in neurogenesis. Overall, these experiments suggest that in human cells, estrogen affects NPC biology and can suppress the convergent ASD-relevant phenotype.

Finally, to test whether estrogen inhibits SHH signaling similarly in human neurons, we used published data to identify DEX genes following estrogen treatment of primary neurons and glia from human PCW6–PCW10 samples (Csöregi et al., 2009). Key SHH signaling targets *NKX2.1*, *DLX2*, *LHX6*, and *DLX5* (Tanabe and Jessell, 1996; Ericson et al., 1997; Hamerschmidt et al., 1997) were repressed (Figure 8G; Table S6). Compared with the *Xenopus* estrogen treatment data, 68 of the 82 (83%) commonly affected genes changed in the same

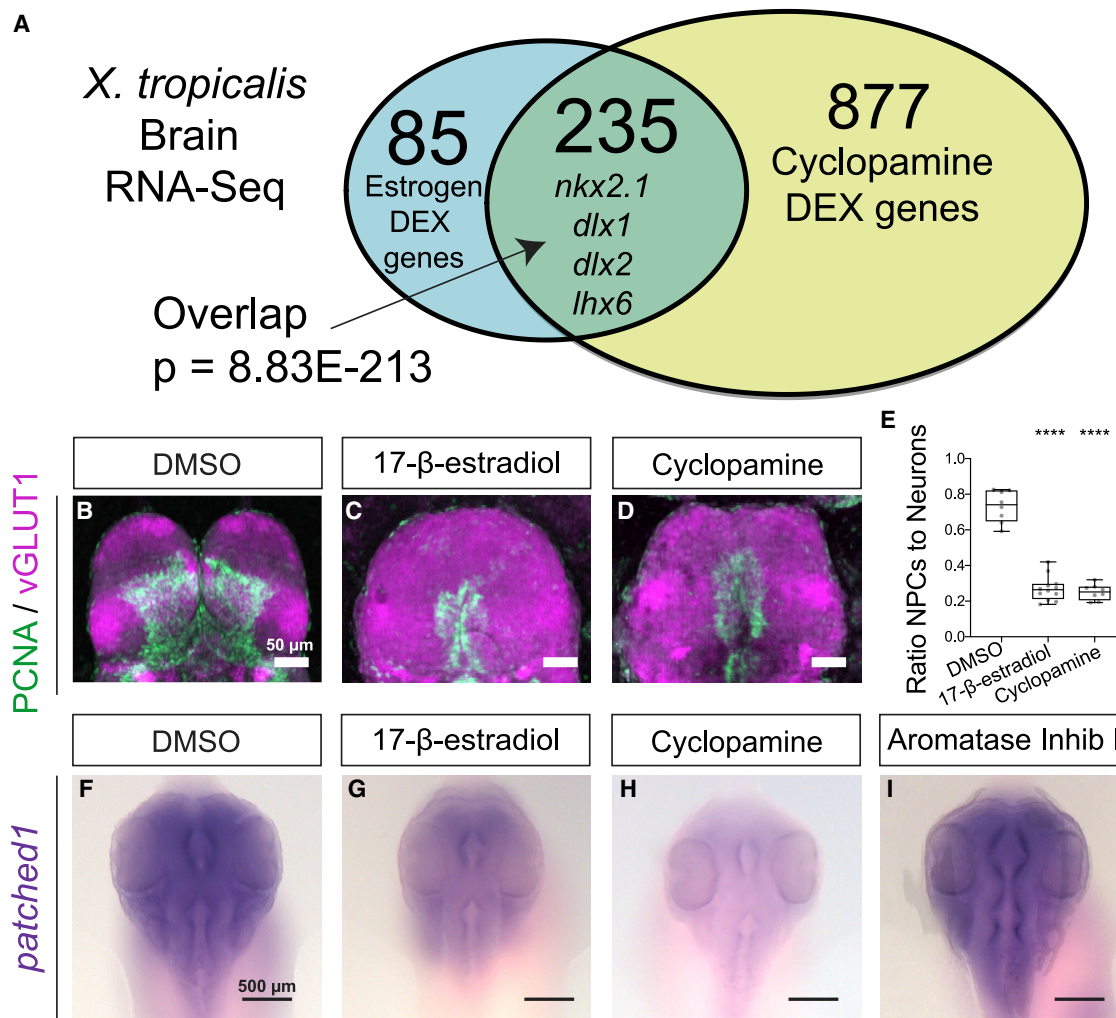


Figure 7. Estrogen signaling inhibits Sonic hedgehog signaling

(A) Differentially expressed (DEX) genes (fold change > 2) from RNA-seq of dissected brains following 10 μ M 17- β -estradiol treatment (blue) or 5 μ M cyclopamine treatment (yellow), showing significant ($p < 0.0001$, hypergeometric test) overlap of DEX genes (green) in the same direction.

(B–D) Treatment with 10 μ M 17- β -estradiol (C) or 5 μ M cyclopamine (D) causes a marked reduction in the ratio of NPCs (PCNA, green) to neurons (vGlut1, magenta) and midline defects in the telencephalon, compared to DMSO control (B).

(E) Quantification of (B)–(D). Mann-Whitney test, **** $p < 0.0001$.

(F and G) Treatment with 20 μ M 17- β -estradiol (G) reduces SHH target gene *patched1* expression compared with control DMSO (F).

(H and I) Positive control 10 μ M cyclopamine (H) reduces *patched1* expression, whereas 50 μ M aromatase inhibitor increases it (I).

direction, including the same key SHH targets (Figure 8G). Altogether, these results suggest that the role of estrogen in inhibiting SHH signaling is conserved in human-derived models of brain development and in human primary tissue.

DISCUSSION

Overall, using a parallelized experimental framework simultaneously assessing ten hcASD risk genes, we have identified a nexus of *in vivo* phenotypic convergence in telencephalon neurogenesis. This work expands the universe of points of overlap in ASD from GO analyses putatively implicating synapse and chromatin to include neurogenesis and neural progenitor matu-

ration, as has been hypothesized by others (Packer, 2016). Key to this discovery is unilateral mutagenesis in *X. tropicalis*, which allows the comparison of mutant and control halves of the brain within the same animal, enabling detection of subtle size changes that might have been missed in model systems that require interanimal comparisons. The location and timing of this phenomenon in *Xenopus* correspond to a key point of spatial, temporal, and cellular-level convergence highlighted in prior studies of ASD risk gene expression in humans (Willsey et al., 2013; Parikshak et al., 2013). Here we extend that work, confirming ASD risk gene convergence within cortical neurons while newly highlighting convergence within the SVZi during human brain development, supporting the idea that multiple points

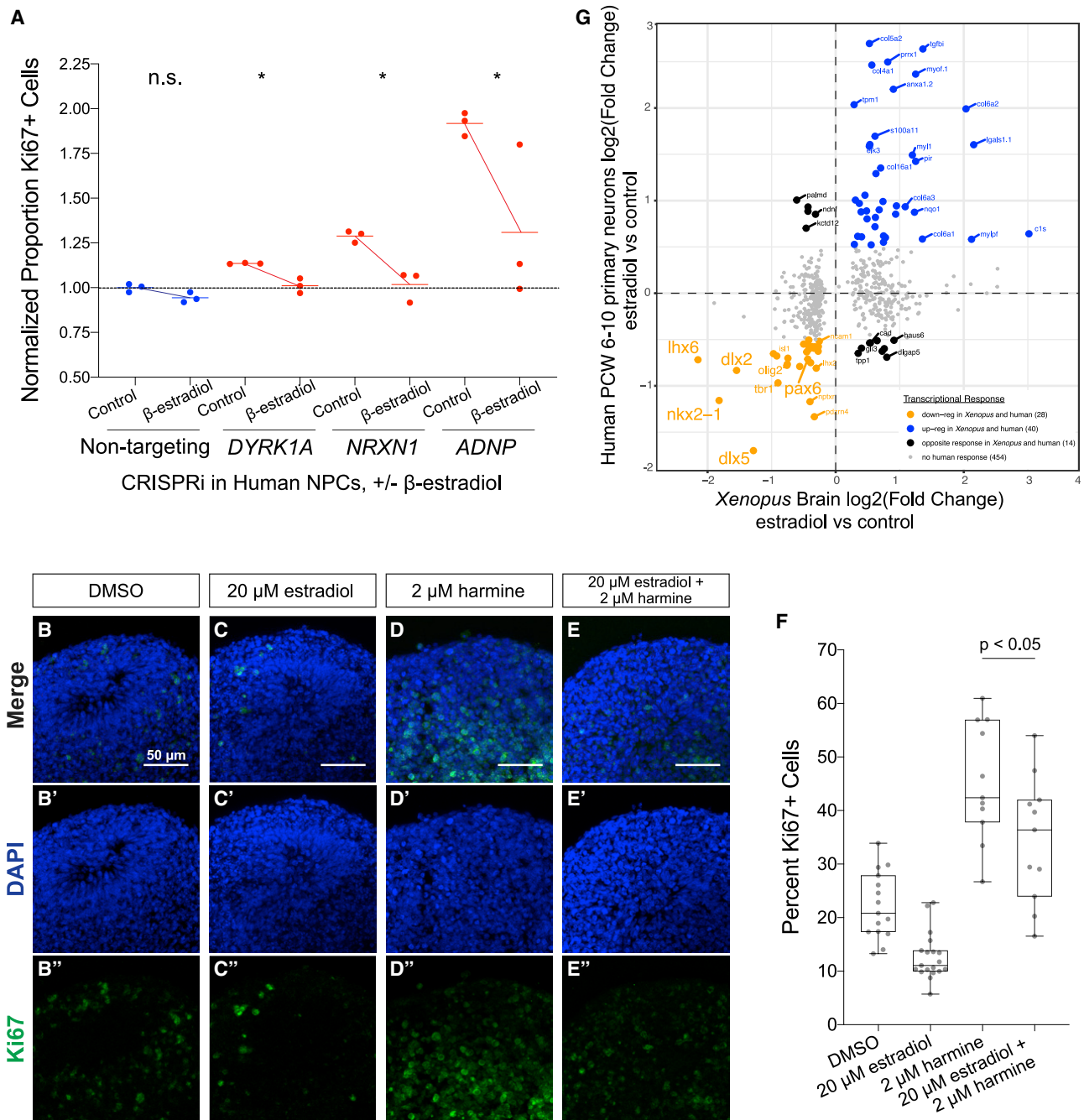


Figure 8. The role of estrogen is conserved in models of human brain development

(A) Quantification of the normalized percentage of Ki67⁺ human NPCs following CRISPRi and treatment with DMSO (control) or 5 μ M 17- β -estradiol. Statistical comparisons are nonparametric Mann-Whitney rank-sum tests, * $p < 0.05$.

(B–E) 5-week-old human iPSC-derived cortical organoids treated with DMSO (B) or with 20 μ M 17- β -estradiol (C), 2 μ M harmine (D), or both (E) for 7 days, stained for DAPI (blue, nuclei) and Ki67 (green, proliferating cells).

(F) Percentage of Ki67⁺ cells. The p value is from a Mann-Whitney test.

(G) Log₂ fold change expression for DEX genes from 17- β -estradiol treatment in *Xenopus* brain versus in human PCW6–PCW10 primary neurons. Blue and orange genes are those that change in the same direction in both species. Black genes are those that change in opposite directions. Gray dots are those that change in *Xenopus*, but not in human neurons.

of convergence will help illuminate core mechanisms, cell types, and circuits underlying ASD. Cells in the SVZ are highly proliferative and neurogenic, providing clear hypotheses about how disrupting these cells may alter forebrain size. Targeted disruption of multiple ASD risk genes of diverse cellular functions in human iPSC-derived NPCs altered the proportion of actively dividing cells. Our findings are generally consistent with a series of individual findings across multiple model systems observing brain size changes for individual ASD risk gene perturbations (Bernier et al., 2014; Hoffman et al., 2016; Zhao et al., 2017; Willsey et al., 2020; Durak et al., 2016; Shen et al., 2015; Katayama et al., 2016) and with clinical observations of gross changes in head size in some individuals with ASD, including in those carrying variants in genes studied here, for example, *CHD8*, *DYRK1A*, and *POGZ* (Ji et al., 2015; Evers et al., 2017; van Bon et al., 2016; Yasin et al., 2019; Bernier et al., 2014; O’Roak et al., 2012a; Ye et al., 2015). The direction and magnitude of forebrain size changes likely depend on the strength of the genetic perturbation, the developmental stage at which size is assayed, and the molecular function of the gene. For example, here we observe *chd8* *Xenopus* mutants have, on average, smaller telencephalons, whereas patients with *CHD8* haploinsufficiency exhibit macrocephaly (Ji et al., 2015; Evers et al., 2017; van Bon et al., 2016; Yasin et al., 2019; Bernier et al., 2014; O’Roak et al., 2012a; Ye et al., 2015). It is well-established that affecting NPC biology during neurogenesis can lead to increased or decreased brain size (Shao et al., 2020; Faheem et al., 2015; Lasser et al., 2018). For example, a delay in differentiation could cause a relative increase in NPCs that could resolve as a larger brain. Alternatively, a delay in cell-cycle progression could cause a relative increase in NPCs but lead to a smaller brain. Indeed, *dyrk1a* inhibition leads to mitotic arrest and cell death in *Xenopus* (Willsey et al., 2020), which could explain the relative increase in NPC proportion despite smaller brain size. Important future work will be to determine additional specific mechanisms for why we observe a relative increase in NPCs regardless of whether an increase or a decrease in telencephalon size is observed. Similarly, it will be informative to determine whether loss of specific ASD risk genes affects diverse telencephalic NPC populations differently, such as dorsal and ventral NPCs.

It may have been anticipated that chromatin modifiers would influence the developmental trajectory of neural progenitors. However, the same observation for genes historically annotated with synaptic/neuronal function, including *SCN2A*, *NRXN1*, *SYNGAP1*, and *ANK2*, is more surprising. A primary motivation for conducting manipulations of multiple ASD risk genes in parallel *in vivo* is to allow the identification of points of convergence that are not bound by the constraints of existing annotation schemes.

A lingering question in the study of ASD risk genes is whether elaboration of underlying biological mechanisms holds promise for illuminating the etiology of social impairment versus more global cognitive delay. The salience of this issue is underscored by the observation that many genes that increase ASD risk may lead to a range of sometimes co-morbid neurodevelopmental disorders, including, commonly, intellectual disability (ID). Recently, study cohorts have grown sufficiently large to allow the preliminary categorization of risk genes into those more

frequently associated with ASD versus those more commonly associated with both ASD and ID (Satterstrom et al., 2020). Referencing these findings, three genes studied here fall into the ASD predominant group (*CHD8*, *NRXN1*, and *ANK2*) and the remainder fall into the ASD and neurodevelopmental delay group (*SCN2A*, *ARID1B*, *DYRK1A*, *SYNGAP1*, *CHD2*, *ANDP*, and *POGZ*). Consequently, we have identified a conserved, convergent phenotype that is highly likely to be relevant to social deficits and possibly relevant to cognitive disability in humans. This finding is consistent with a range of observations suggesting that the diversity of human neurodevelopmental phenotypes associated with a given gene is not likely determined solely at the level of the mutation but may be a consequence of several mechanisms, including common polygenic background, stochastic events, and environmental factors (State and Levitt, 2011). However, although our findings do not disentangle the complex interrelationship between ID and ASD, our results cannot be easily ascribed to the inadvertent study of a group of genes that increase ASD risk only as a byproduct of more global ID in humans.

Finally, we used chemical screening to identify potential resilience factors, with the hypothesis that they may protect against mutations in multiple ASD risk genes by rescuing the convergent higher level phenotype and may not necessarily directly intersect the individual molecular mechanisms of each gene. This approach identified estrogen as a suppressor of the convergent neurogenesis phenotype in both *Xenopus* and human models, across multiple apparently functionally disparate risk genes, suggesting that it is a more general resilience factor. Again, because the molecular mechanisms leading to defects in neurogenesis may be different across the diverse set of ASD risk genes, we hypothesize that estrogen is providing resilience through modulation of neurogenesis, rather than rescuing molecular deficits specific to each gene. We elaborated a novel role for estrogen in opposing SHH signaling in the developing telencephalon. SHH signaling is known to play critical and well-established roles in regulating dorsal-ventral patterning, proliferation, progenitor cell maturation, and cell survival throughout the telencephalon during brain development (Britto et al., 2002; Echelard et al., 1993; Komada et al., 2008), as well as in the context of cancer (Wu et al., 2017). Therefore, these findings point to novel and testable hypotheses regarding the potential roles of these pathways in brain development and in modulating ASD risk. In particular, the potential for estrogen signaling to influence sexual dimorphism raises salient questions about the strong male sex bias observed in ASD, as well as sex biases observed in other human disorders, especially those with a strong influence of SHH signaling.

STAR★METHODS

Detailed methods are provided in the online version of this paper and include the following:

- KEY RESOURCES TABLE
- RESOURCE AVAILABILITY
 - Lead contact
 - Materials availability

- Data and code availability
- **EXPERIMENTAL MODEL AND SUBJECT DETAILS**
 - Animal models
 - Cell lines
- **METHOD DETAILS**
 - Obtaining *Xenopus tropicalis* embryos and tadpoles
 - *Xenopus* whole mount RNA *in situ* hybridization
 - *Xenopus* brain time-course transcriptomics
 - *Xenopus tropicalis* microinjections
 - *Xenopus* CRISPR/Cas9 genome editing
 - *Xenopus* genotyping
 - *Xenopus* whole mount immunofluorescence
 - *Xenopus* microscopy
 - *Xenopus* brain size measurements
 - CRISPRi experiments in human NPCs
 - Human CRISPRi NPC proportion quantification
 - PCNet hcASD gene interconnectivity analysis
 - Constructing hcASD networks
 - BrainSpan layer-specific data
 - PCNet average gene connectivity
 - BrainSpan layer-specific hcASD network connectivity analysis
 - *Xenopus* small molecule treatments
 - *Xenopus* drug treatment transcriptomics
 - Human CRISPRi NPC estrogen treatment
 - Organoid generation and drug treatment
 - Organoid staining & imaging
 - Human PCW6-10 transcriptome analysis & comparison to *Xenopus*
 - *ESR2* CRISPRi in NPCs
 - *ESR2* CRISPRi transcriptomic analysis
- **QUANTIFICATION AND STATISTICAL ANALYSIS**
- **ADDITIONAL RESOURCES**

SUPPLEMENTAL INFORMATION

Supplemental Information can be found online at <https://doi.org/10.1016/j.neuron.2021.01.002>.

ACKNOWLEDGMENTS

We thank John Rubenstein for critical reading; Brian Shoichet for expertise on chemical inhibitors; Mustafa Khokha and Michael Slocum for wild-type frogs and husbandry expertise; Gary Moulder, Nolan Wong, Kelly Jensen, Shaun Coughlin, Kristina Lindstrom, Louie Ramos, and Mary Casis for support at the UCSF *Xenopus* facility; James Evans for support at the UC Berkeley *Xenopus* facility; Emily Mis, Karen Liu, Maura Lane, and Edivinia Pangilinan for expert technical help; Bruce Conklin, Michael Ward, and Martin Kampmann for sharing WTC iPSC lines and protocols; CSHL *Xenopus* courses (2015–2019); the UC Berkeley Functional Genomics Laboratory; Xenbase (RRID: SCR_003280); National *Xenopus* Resource (RRID: SCR_013731); Sarah Pyle for graphic design; and the Vincent J. Coates Genomics Sequencing Laboratory, supported by NIH S10 OD018174. We thank the Weill Institute for Neurosciences. This work was supported by a gift from the Overlook International Foundation and grant support from the National Institutes of Mental Health Convergent Neuroscience Initiative and the Psychiatric Cell Map Initiative (pcmi.ucsf.edu, 1U01MH115747-01A1) to A.J.W. and M.W.S., as well as grants from the National Institutes of Mental Health (1R21MH112158-01) to R.M.H. and the National Institute of General Medical Sciences (R35GM127069) to R.M.H.

AUTHOR CONTRIBUTIONS

Conceptualization, H.R.W., A.J.W., M.W.S., and R.M.H.; Experiments, H.R.W., C.R.T.E., Y.X., A.E., J.D., G.S., N.S., Y.Z., N.T., A.K., A.S.A., D.S., and M.S.; Computational analyses, A.E., B.W., and A.J.W.; Data interpretation, H.R.W., C.R.T.E., Y.X., A.E., B.W., A.J.W., M.W.S., and R.M.H.; Writing – original draft, H.R.W.; Writing – review & editing, M.W.S., A.J.W., and R.M.H.

DECLARATION OF INTERESTS

M.W.S. is a consultant for RBNC Therapeutics.

Received: May 25, 2020

Revised: December 2, 2020

Accepted: January 4, 2021

Published: January 25, 2021; Corrected online: March 31, 2021

REFERENCES

- Anderson, S.A., Qiu, M., Bulfone, A., Eisenstat, D.D., Meneses, J., Pedersen, R., and Rubenstein, J.L. (1997). Mutations of the homeobox genes *Dlx-1* and *Dlx-2* disrupt the striatal subventricular zone and differentiation of late born striatal neurons. *Neuron* 19, 27–37.
- Ben-David, E., and Shifman, S. (2013). Combined analysis of exome sequencing points toward a major role for transcription regulation during brain development in autism. *Mol. Psychiatry* 18, 1054–1056.
- Bernier, R., Golzio, C., Xiong, B., Stessman, H.A., Coe, B.P., Penn, O., Witherspoon, K., Gerdts, J., Baker, C., Vulto-van Silfhout, A.T., et al. (2014). Disruptive *CHD8* mutations define a subtype of autism early in development. *Cell* 158, 263–276.
- Bhattacharya, D., Marfo, C.A., Li, D., Lane, M., and Khokha, M.K. (2015). CRISPR/Cas9: An inexpensive, efficient loss of function tool to screen human disease genes in *Xenopus*. *Dev. Biol.* 408, 196–204.
- Blackburn, A.T.M., Bekheirnia, N., Uma, V.C., Rosenfeld, J.A., Bainbridge, M.N., Yang, Y., Liu, P., et al. (2019). *DYRK1A*-Related Intellectual Disability: A Syndrome Associated with Congenital Anomalies of the Kidney and Urinary Tract. *Genet. Med.* 21, 2755–2764.
- Brinkman, E.K., Chen, T., Amendola, M., and van Steensel, B. (2014). Easy quantitative assessment of genome editing by sequence trace decomposition. *Nucleic Acids Res.* 42, e168.
- Britto, J., Tannahill, D., and Keynes, R. (2002). A critical role for sonic hedgehog signaling in the early expansion of the developing brain. *Nat. Neurosci.* 5, 103–110.
- Chang, J., Gilman, S.R., Chiang, A.H., Sanders, S.J., and Vitkup, D. (2015). Genotype to phenotype relationships in autism spectrum disorders. *Nat. Neurosci.* 18, 191–198.
- Chen, J.K., Taipale, J., Cooper, M.K., and Beachy, P.A. (2002). Inhibition of Hedgehog signaling by direct binding of cyclopamine to Smoothened. *Genes Dev.* 16, 2743–2748.
- Chen, B., Gilbert, L.A., Cimini, B.A., Schnitzbauer, J., Zhang, W., Li, G.-W., Park, J., Blackburn, E.H., Weissman, J.S., Qi, L.S., and Huang, B. (2013). Dynamic imaging of genomic loci in living human cells by an optimized CRISPR/Cas system. *Cell* 155, 1479–1491.
- Chiang, C., Litingtung, Y., Lee, E., Young, K.E., Corden, J.L., Westphal, H., and Beachy, P.A. (1996). Cyclopia and defective axial patterning in mice lacking Sonic hedgehog gene function. *Nature* 383, 407–413.
- Csöreg, L., Andersson, E., and Fried, G. (2009). Transcriptional analysis of estrogen effects in human embryonic neurons and glial cells. *Neuroendocrinology* 89, 171–186.
- De Rubeis, S., He, X., Goldberg, A.P., Poultney, C.S., Samocha, K., Cicek, A.E., Kou, Y., Liu, L., Fromer, M., Walker, S., et al.; DDD Study; Homozygosity Mapping Collaborative for Autism; UK10K Consortium (2014). Synaptic, transcriptional and chromatin genes disrupted in autism. *Nature* 515, 209–215.

- DeLay, B.D., Corkins, M.E., Hanania, H.L., Salanga, M., Jian, M.D., Sudou, N., Taira, M., Horb, M.E., and Miller, R.K. (2018). Tissue-Specific Gene Inactivation in: Knockout of in the Kidney with CRISPR/Cas9. *Genetics* 208, 673–686.
- Deniz, E., Mis, E.K., Lane, M., and Khokha, M.K. (2018). CRISPR/Cas9 F0 Screening of Congenital Heart Disease Genes in *Xenopus tropicalis*. *Methods Mol. Biol.* 1865, 163–174.
- Dobin, A., Davis, C.A., Schlesinger, F., Drenkow, J., Zaleski, C., Jha, S., Batut, P., Chaisson, M., and Gingeras, T.R. (2013). STAR: ultrafast universal RNA-seq aligner. *Bioinformatics* 29, 15–21.
- Duncan, A.R., and Khokha, M.K. (2016). *Xenopus* as a model organism for birth defects—Congenital heart disease and heterotaxy. *Semin. Cell Dev. Biol.* 51, 73–79.
- Durak, O., Gao, F., Kaeser-Woo, Y.J., Rueda, R., Martorell, A.J., Nott, A., Liu, C.Y., Watson, L.A., and Tsai, L.-H. (2016). Chd8 mediates cortical neurogenesis via transcriptional regulation of cell cycle and Wnt signaling. *Nat. Neurosci.* 19, 1477–1488.
- Echelard, Y., Epstein, D.J., St-Jacques, B., Shen, L., Mohler, J., McMahon, J.A., and McMahon, A.P. (1993). Sonic hedgehog, a member of a family of putative signaling molecules, is implicated in the regulation of CNS polarity. *Cell* 75, 1417–1430.
- Edgar, R., Domrachev, M., and Lash, A.E. (2002). Gene Expression Omnibus: NCBI gene expression and hybridization array data repository. *Nucleic Acids Res.* 30, 207–210.
- Ericson, J., Muhr, J., Placzek, M., Lints, T., Jessell, T.M., and Edlund, T. (1995). Sonic hedgehog induces the differentiation of ventral forebrain neurons: a common signal for ventral patterning within the neural tube. *Cell* 81, 747–756.
- Ericson, J., Briscoe, J., Rashbass, P., van Heyningen, V., and Jessell, T.M. (1997). Graded sonic hedgehog signaling and the specification of cell fate in the ventral neural tube. *Cold Spring Harb. Symp. Quant. Biol.* 62, 451–466.
- Etard, C., Joshi, S., Stegmaier, J., Mikut, R., and Strähle, U. (2017). Tracking of Indels by DEcomposition is a Simple and Effective Method to Assess Efficiency of Guide RNAs in Zebrafish. *Zebrafish* 14, 586–588.
- Evers, J.M.G., Laskowski, R.A., Bertoli, M., Clayton-Smith, J., Deshpande, C., Eason, J., Eimslie, F., Flintner, F., Gardiner, C., Hurst, J.A., et al.; DDD Study (2017). Structural analysis of pathogenic mutations in the DYRK1A gene in patients with developmental disorders. *Hum. Mol. Genet.* 26, 519–526.
- Exner, C.R.T., and Willsey, H.R. (2020). *Xenopus* leads the way: Frogs as a pioneering model to understand the human brain. *Genesis*. <https://doi.org/10.1002/dvg.23405>.
- Faheem, M., Naseer, M.I., Rasool, M., Chaudhary, A.G., Kumosani, T.A., Ilyas, A.M., Pushparaj, P., Ahmed, F., Algahtani, H.A., Al-Qahtani, M.H., and Saleh Jamal, H. (2015). Molecular genetics of human primary microcephaly: an overview. *BMC Med. Genomics* 8 (Suppl 1), S4.
- Fuccillo, M., Rallu, M., McMahon, A.P., and Fishell, G. (2004). Temporal requirement for hedgehog signaling in ventral telencephalic patterning. *Development* 131, 5031–5040.
- Gallego Romero, I., Pavlovic, B.J., Hernando-Herraez, I., Zhou, X., Ward, M.C., Banovich, N.E., Kagan, C.L., Burnett, J.E., Huang, C.H., Mitrano, A., et al. (2015). A panel of induced pluripotent stem cells from chimpanzees: a resource for comparative functional genomics. *eLife* 4, e07103.
- Garfinkel, A.M., and Khokha, M.K. (2017). An interspecies heart-to-heart: Using *Xenopus* to uncover the genetic basis of congenital heart disease. *Curr. Pathobiol. Rep.* 5, 187–196.
- Göckler, N., Jofre, G., Papadopoulos, C., Soppa, U., Tejedor, F.J., and Becker, W. (2009). Harmine specifically inhibits protein kinase DYRK1A and interferes with neurite formation. *FEBS J.* 276, 6324–6337.
- Hammerschmidt, M., Brook, A., and McMahon, A.P. (1997). The world according to hedgehog. *Trends Genet.* 13, 14–21.
- Harland, R.M. (1991). *In Situ* Hybridization: An Improved Whole-Mount Method for *Xenopus* Embryos. *Methods Cell Biol.* 36, 685–695.
- Hoffman, E.J., Turner, K.J., Fernandez, J.M., Cifuentes, D., Ghosh, M., Ijaz, S., Jain, R.A., Kubo, F., Bill, B.R., Baier, H., et al. (2016). Estrogens Suppress a Behavioral Phenotype in Zebrafish Mutants of the Autism Risk Gene, CNTNAP2. *Neuron* 89, 725–733.
- Horlbeck, M.A., Gilbert, L.A., Villalta, J.E., Adamson, B., Pak, R.A., Chen, Y., Fields, A.P., Park, C.Y., Corn, J.E., Kampmann, M., and Weissman, J.S. (2016). Compact and highly active next-generation libraries for CRISPR-mediated gene repression and activation. *eLife* 5, e19760.
- Huang, J.K., Carlin, D.E., Yu, M.K., Zhang, W., Kreisberg, J.F., Tamayo, P., and Ideker, T. (2018). Systematic Evaluation of Molecular Networks for Discovery of Disease Genes. *Cell Syst.* 6, 484–495.e5.
- Iossifov, I., Ronemus, M., Levy, D., Wang, Z., Hakker, I., Rosenbaum, J., Yamrom, B., Lee, Y.H., Narzisi, G., Leotta, A., et al. (2012). *De novo* gene disruptions in children on the autistic spectrum. *Neuron* 74, 285–299.
- Iossifov, I., O’Roak, B.J., Sanders, S.J., Ronemus, M., Krumm, N., Levy, D., Stessman, H.A., Witherspoon, K.T., Vives, L., Patterson, K.E., et al. (2014). The contribution of *de novo* coding mutations to autism spectrum disorder. *Nature* 515, 216–221.
- Ji, J., Lee, H., Argiropoulos, B., Dorrani, N., Mann, J., Martinez-Agosto, J.A., Gomez-Ospina, N., Gallant, N., Bernstein, J.A., Hudgins, L., et al. (2015). DYRK1A haploinsufficiency causes a new recognizable syndrome with microcephaly, intellectual disability, speech impairment, and distinct facies. *Eur. J. Hum. Genet.* 23, 1473–1481.
- Jin, S.C., Homsy, J., Zaidi, S., Lu, Q., Morton, S., DePalma, S.R., Zeng, X., Qi, H., Chang, W., Sierant, M.C., et al. (2017). Contribution of rare inherited and *de novo* variants in 2,871 congenital heart disease probands. *Nat. Genet.* 49, 1593–1601.
- Kekebeen, A., and Wills, A. (2019). Advancing genetic and genomic technologies deepen the pool for discovery in *Xenopus tropicalis*. *Dev. Dyn.* 248, 620–625.
- Kang, H.J., Kawasawa, Y.I., Cheng, F., Zhu, Y., Xu, X., Li, M., Sousa, A.M.M., Pletikos, M., Meyer, K.A., Sedmak, G., et al. (2011). Spatio-temporal transcriptome of the human brain. *Nature* 478, 483–489.
- Katayama, Y., Nishiyama, M., Shoji, H., Ohkawa, Y., Kawamura, A., Sato, T., Suyama, M., Takumi, T., Miyakawa, T., and Nakayama, K.I. (2016). CHD8 haploinsufficiency results in autistic-like phenotypes in mice. *Nature* 537, 675–679.
- Koebernick, K., Hollemann, T., and Pieler, T. (2001). Molecular cloning and expression analysis of the Hedgehog receptors XPTc1 and XSmo in *Xenopus laevis*. *Mech. Dev.* 100, 303–308.
- Komada, M., Saito, H., Kinboshi, M., Miura, T., Shiota, K., and Ishibashi, M. (2008). Hedgehog signaling is involved in development of the neocortex. *Development* 135, 2717–2727.
- Kriegstein, A., Noctor, S., and Martínez-Cerdeño, V. (2006). Patterns of neural stem and progenitor cell division may underlie evolutionary cortical expansion. *Nat. Rev. Neurosci.* 7, 883–890.
- Krneta-Stankic, V., DeLay, B.D., and Miller, R.K. (2017). *Xenopus*: leaping forward in kidney organogenesis. *Pediatr. Nephrol.* 32, 547–555.
- Lasser, M., Tiber, J., and Lowery, L.A. (2018). The Role of the Microtubule Cytoskeleton in Neurodevelopmental Disorders. *Front. Cell. Neurosci.* 12, 165.
- Lewis, C., and Krieg, P.A. (2014). Reagents for developmental regulation of Hedgehog signaling. *Methods* 66, 390–397.
- Li, J., Ma, Z., Shi, M., Maly, R.H., Aoki, H., Minic, Z., Phanse, S., Jin, K., Wall, D.P., Zhang, Z., et al. (2015). Identification of Human Neuronal Protein Complexes Reveals Biochemical Activities and Convergent Mechanisms of Action in Autism Spectrum Disorders. *Cell Syst.* 1, 361–374.
- A. Lieberman, C.W. Olanow, M.B.H. Youdim, and K. Tipton, eds. (1994). *Monoamine Oxidase Inhibitors in Neurological Diseases* (CRC Press).
- Love, M.I., Huber, W., and Anders, S. (2014). Moderated estimation of fold change and dispersion for RNA-seq data with DESeq2. *Genome Biol.* 15, 550.
- Mandegar, M.A., Huebsch, N., Frolov, E.B., Shin, E., Truong, A., Olvera, M.P., Chan, A.H., Miyaoka, Y., Holmes, K., Spencer, C.I., et al. (2016). CRISPR Interference Efficiently Induces Specific and Reversible Gene Silencing in Human iPSCs. *Cell Stem Cell* 18, 541–553.

- Martínez-Cerdeño, V., Noctor, S.C., and Kriegstein, A.R. (2006). The role of intermediate progenitor cells in the evolutionary expansion of the cerebral cortex. *Cereb. Cortex* 16 (Suppl 1), i152–i161.
- Matsumoto, Y., Hayashi, Y., Schlieve, C.R., Ikeya, M., Kim, H., Nguyen, T.D., Sami, S., Baba, S., Barriet, E., Nasu, A., et al. (2013). Induced pluripotent stem cells from patients with human fibrodysplasia ossificans progressiva show increased mineralization and cartilage formation. *Orphanet J. Rare Dis.* 8, 190.
- Mi, H., Dong, Q., Muruganujan, A., Gaudet, P., Lewis, S., and Thomas, P.D. (2010). PANTHER version 7: improved phylogenetic trees, orthologs and collaboration with the Gene Ontology Consortium. *Nucleic Acids Res.* 38, D204–D210.
- Miller, J.A., Ding, S.-L., Sunkin, S.M., Smith, K.A., Ng, L., Szafer, A., Ebbert, A., Riley, Z.L., Royall, J.J., Aiona, K., et al. (2014). Transcriptional landscape of the prenatal human brain. *Nature* 508, 199–206.
- Moreno-Mateos, M.A., Vejnar, C.E., Beaudoin, J.-D., Fernandez, J.P., Mis, E.K., Khokha, M.K., and Giraldez, A.J. (2015). CRISPRscan: designing highly efficient sgRNAs for CRISPR-Cas9 targeting *in vivo*. *Nat. Methods* 12, 982–988.
- Morin, R.D., Chang, E., Petrescu, A., Liao, N., Griffith, M., Chow, W., Kirkpatrick, R., Butterfield, Y.S., Young, A.C., Stott, J., et al. (2006). Sequencing and analysis of 10,967 full-length cDNA clones from *Xenopus laevis* and *Xenopus tropicalis* reveals post-tetraploidization transcriptome remodeling. *Genome Res.* 16, 796–803.
- Neale, B.M., Kou, Y., Liu, L., Ma'ayan, A., Samocha, K.E., Sabo, A., Lin, C.-F., Stevens, C., Wang, L.S., Makarov, V., et al. (2012). Patterns and rates of exonic *de novo* mutations in autism spectrum disorders. *Nature* 485, 242–245.
- Nieber, F., Pieler, T., and Henningfeld, K.A. (2009). Comparative expression analysis of the neurogenins in *Xenopus tropicalis* and *Xenopus laevis*. *Dev. Dyn.* 238, 451–458.
- Nieuwkoop, P.D., and Faber, J. (1994). *Normal Table of Xenopus laevis* Volume 43 (Garland Publishing, Inc.).
- O'Roak, B.J., Vives, L., Fu, W., Egerton, J.D., Stanaway, I.B., Phelps, I.G., Carvill, G., Kumar, A., Lee, C., Ankenman, K., et al. (2012a). Multiplex targeted sequencing identifies recurrently mutated genes in autism spectrum disorders. *Science* 338, 1619–1622.
- O'Roak, B.J., Vives, L., Girirajan, S., Karakoc, E., Krumm, N., Coe, B.P., Levy, R., Ko, A., Lee, C., Smith, J.D., et al. (2012b). Sporadic autism exomes reveal a highly interconnected protein network of *de novo* mutations. *Nature* 485, 246–250.
- Ogawa, Y., Nonaka, Y., Goto, T., Ohnishi, E., Hiramatsu, T., Kii, I., Yoshida, M., Ikura, T., Onogi, H., Shibuya, H., et al. (2010). Development of a novel selective inhibitor of the Down syndrome-related kinase Dyrk1A. *Nat. Commun.* 1, 86.
- Ohkubo, Y., Chiang, C., and Rubenstein, J.L.R. (2002). Coordinate regulation and synergistic actions of BMP4, SHH and FGF8 in the rostral prosencephalon regulate morphogenesis of the telencephalic and optic vesicles. *Neuroscience* 111, 1–17.
- Ortega, J.A., Memi, F., Radonjic, N., Filipovic, R., Bagasrawala, I., Zecevic, N., and Jakovcevski, I. (2018). The Subventricular Zone: A Key Player in Human Neocortical Development. *Neuroscientist* 24, 156–170.
- Packer, A. (2016). Neocortical neurogenesis and the etiology of autism spectrum disorder. *Neurosci. Biobehav. Rev.* 64, 185–195.
- Parikshak, N.N., Luo, R., Zhang, A., Won, H., Lowe, J.K., Chandran, V., Horvath, S., and Geschwind, D.H. (2013). Integrative functional genomic analyses implicate specific molecular pathways and circuits in autism. *Cell* 155, 1008–1021.
- Paşca, A.M., Sloan, S.A., Clarke, L.E., Tian, Y., Makinson, C.D., Huber, N., Kim, C.H., Park, J.Y., O'Rourke, N.A., Nguyen, K.D., et al. (2015). Functional cortical neurons and astrocytes from human pluripotent stem cells in 3D culture. *Nat. Methods* 12, 671–678.
- Pearl, E.J., Grainger, R.M., Guille, M., and Horb, M.E. (2012). Development of *Xenopus* resource centers: the National *Xenopus* Resource and the European *Xenopus* Resource Center. *Genesis* 50, 155–163.
- Qi, Y., Zhang, X.-J., Renier, N., Wu, Z., Atkin, T., Sun, Z., Ozair, M.Z., Tchiew, J., Zimmer, B., Fattahi, F., et al. (2017). Combined small-molecule inhibition accelerates the derivation of functional cortical neurons from human pluripotent stem cells. *Nat. Biotechnol.* 35, 154–163.
- Ruzzo, E.K., Pérez-Cano, L., Jung, J.-Y., Wang, L.-K., Kashef-Haghighi, D., Hartl, C., Singh, C., Xu, J., Hoekstra, J.N., Leventhal, O., et al. (2019). Inherited and *De Novo* Genetic Risk for Autism Impacts Shared Networks. *Cell* 178, 850–866.e26.
- Sakai, Y., Shaw, C.A., Dawson, B.C., Dugas, D.V., Al-Mohtaseb, Z., Hill, D.E., and Zoghbi, H.Y. (2011). Protein interactome reveals converging molecular pathways among autism disorders. *Sci. Transl. Med.* 3, 86ra49.
- Sanders, S.J., Murtha, M.T., Gupta, A.R., Murdoch, J.D., Raubeson, M.J., Willsey, A.J., Ercan-Sencicek, A.G., DiLullo, N.M., Parikshak, N.N., Stein, J.L., et al. (2012). *De novo* mutations revealed by whole-exome sequencing are strongly associated with autism. *Nature* 485, 237–241.
- Sanders, S.J., He, X., Willsey, A.J., Ercan-Sencicek, A.G., Samocha, K.E., Cicek, A.E., Murtha, M.T., Bal, V.H., Bishop, S.L., Dong, S., et al.; Autism Sequencing Consortium (2015). Insights into Autism Spectrum Disorder Genomic Architecture and Biology from 71 Risk Loci. *Neuron* 87, 1215–1233.
- Satterstrom, F.K., Kosmicki, J.A., Wang, J., Breen, M.S., De Rubeis, S., An, J.-Y., Peng, M., Collins, R., Grove, J., Klei, L., et al.; Autism Sequencing Consortium; iPSYCH-Broad Consortium (2020). Large-Scale Exome Sequencing Study Implicates Both Developmental and Functional Changes in the Neurobiology of Autism. *Cell* 180, 568–584.e23.
- Schindelin, J., Arganda-Carreras, I., Frise, E., Kaynig, V., Longair, M., Pietzsch, T., Preibisch, S., Rueden, C., Saalfeld, S., Schmid, B., et al. (2012). Fiji: an open-source platform for biological-image analysis. *Nat. Methods* 9, 676–682.
- Sestan, N., and State, M.W. (2018). Lost in Translation: Traversing the Complex Path from Genomics to Therapeutics in Autism Spectrum Disorder. *Neuron* 100, 406–423.
- Shao, W., Yang, J., He, M., Yu, X.-Y., Lee, C.H., Yang, Z., Joyner, A.L., Anderson, K.V., Zhang, J., Tsou, M.B., et al. (2020). Centrosome anchoring regulates progenitor properties and cortical formation. *Nature* 580, 106–112.
- Shen, T., Ji, F., Yuan, Z., and Jiao, J. (2015). CHD2 is Required for Embryonic Neurogenesis in the Developing Cerebral Cortex. *Stem Cells* 33, 1794–1806.
- Shimamura, K., and Rubenstein, J.L. (1997). Inductive interactions direct early regionalization of the mouse forebrain. *Development* 124, 2709–2718.
- Sive, H.L., Grainger, R.M., and Harland, R.M. (2007). Baskets for *in Situ* Hybridization and Immunohistochemistry. *CSH Protoc.* 2007, pdb.prot4777.
- Sive, H.L., Grainger, R.M., and Harland, R.M. (2000). *Early Development of Xenopus laevis: A Laboratory Manual* (CSHL Press).
- State, M.W., and Levitt, P. (2011). The conundrums of understanding genetic risks for autism spectrum disorders. *Nat. Neurosci.* 14, 1499–1506.
- State, M.W., and Šestan, N. (2012). Neuroscience. The Emerging Biology of Autism Spectrum Disorders. *Science* 337, 1301–1303.
- Takase, M., and Iguchi, T. (2007). Molecular cloning of two isoforms of *Xenopus* (*Silurana*) *tropicalis* estrogen receptor mRNA and their expression during development. *Biochim. Biophys. Acta* 1769, 172–181.
- Tanabe, Y., and Jessell, T.M. (1996). Diversity and pattern in the developing spinal cord. *Science* 274, 1115–1123.
- Tebbenkamp, A.T.N., Willsey, A.J., State, M.W., and Sestan, N. (2014). The developmental transcriptome of the human brain: implications for neurodevelopmental disorders. *Curr. Opin. Neurol.* 27, 149–156.
- Truchado-Garcia, M., Harland, R.M., and Abrams, M.J. (2018). 3D-Printable Tools for Developmental Biology: Improving Embryo Injection and Screening Techniques through 3D-Printing Technology. *bioRxiv*. <https://doi.org/10.1101/376657>.
- van Bon, B.W.M., Coe, B.P., Bernier, R., Green, C., Gerdts, J., Witherspoon, K., Kleefstra, T., Willemsen, M.H., Kumar, R., Bosco, P., et al. (2016). Disruptive *de novo* mutations of DYRK1A lead to a syndromic form of autism and ID. *Mol. Psychiatry* 21, 126–132.

- Wang, T., Hoekzema, K., Vecchio, D., Wu, H., Sulovari, A., Coe, B.P., Gillentine, M.A., Wilfert, A.B., Perez-Jurado, L.A., Kvarnang, M., et al.; SPARK Consortium (2020). Large-scale targeted sequencing identifies risk genes for neurodevelopmental disorders. *Nat. Commun.* **11**, 4932.
- Willsey, A.J., and State, M.W. (2015). Autism spectrum disorders: from genes to neurobiology. *Curr. Opin. Neurobiol.* **30**, 92–99.
- Willsey, A.J., Sanders, S.J., Li, M., Dong, S., Tebbenkamp, A.T., Muhle, R.A., Reilly, S.K., Lin, L., Fertuzinhos, S., Miller, J.A., et al. (2013). Coexpression networks implicate human midfetal deep cortical projection neurons in the pathogenesis of autism. *Cell* **155**, 997–1007.
- Willsey, A.J., Morris, M.T., Wang, S., Willsey, H.R., Sun, N., Teerikorpi, N., Baum, T.B., Cagney, G., Bender, K.J., Desai, T.A., et al. (2018a). The Psychiatric Cell Map Initiative: A Convergent Systems Biological Approach to Illuminating Key Molecular Pathways in Neuropsychiatric Disorders. *Cell* **174**, 505–520.
- Willsey, H.R., Walentek, P., Exner, C.R.T., Xu, Y., Lane, A.B., Harland, R.M., Heald, R., and Santama, N. (2018b). Katanin-like protein *Katnal2* is required for ciliogenesis and brain development in *Xenopus* embryos. *Dev. Biol.* **442**, 276–287.
- Willsey, H.R., Xu, Y., Everitt, A., Dea, J., Exner, C.R.T., Willsey, A.J., State, M.W., and Harland, R.M. (2020). The neurodevelopmental disorder risk gene *DYRK1A* is required for ciliogenesis and control of brain size in *Xenopus* embryos. *Development* **147**, dev189290.
- Wu, K.H., Tobias, M.L., Thornton, J.W., and Kelley, D.B. (2003). Estrogen receptors in *Xenopus*: duplicate genes, splice variants, and tissue-specific expression. *Gen. Comp. Endocrinol.* **133**, 38–49.
- Wu, F., Zhang, Y., Sun, B., McMahon, A.P., and Wang, Y. (2017). Hedgehog Signaling: From Basic Biology to Cancer Therapy. *Cell Chem. Biol.* **24**, 252–280.
- Xu, X., Wells, A.B., O'Brien, D.R., Nehorai, A., and Dougherty, J.D. (2014). Cell type-specific expression analysis to identify putative cellular mechanisms for neurogenetic disorders. *J. Neurosci.* **34**, 1420–1431.
- Yasin, H., Gibson, W.T., Langlois, S., Stowe, R.M., Tsang, E.S., Lee, L., Poon, J., Tran, G., Tyson, C., Wong, C.K., et al. (2019). A distinct neurodevelopmental syndrome with intellectual disability, autism spectrum disorder, characteristic facies, and macrocephaly is caused by defects in *CHD8*. *J. Hum. Genet.* **64**, 271–280.
- Ye, Y., Cho, M.T., Retterer, K., Alexander, N., Ben-Omran, T., Al-Mureikhi, M., Cristian, I., Wheeler, P.G., Crain, C., Zand, D., et al. (2015). *De novo* POGZ mutations are associated with neurodevelopmental disorders and microcephaly. *Cold Spring Harb. Mol. Case Stud.* **1**, a000455.
- Zecevic, N., Chen, Y., and Filipovic, R. (2005). Contributions of cortical sub-ventricular zone to the development of the human cerebral cortex. *J. Comp. Neurol.* **491**, 109–122.
- Zhao, H., Tu, Z., Xu, H., Yan, S., Yan, H., Zheng, Y., Yang, W., Zheng, J., Li, Z., Tian, R., et al. (2017). Altered neurogenesis and disrupted expression of synaptic proteins in prefrontal cortex of *SHANK3*-deficient non-human primate. *Cell Res.* **27**, 1293–1297.
- Zhu, A., Ibrahim, J.G., and Love, M.I. (2019). Heavy-tailed prior distributions for sequence count data: removing the noise and preserving large differences. *Bioinformatics* **35**, 2084–2092.

STAR★METHODS

KEY RESOURCES TABLE

REAGENT or RESOURCE	SOURCE	IDENTIFIER
Antibodies		
β-Tubulin	DSHB	E7; RRID:AB_528499
PCNA	Life Technologies	PC10; RRID:AB_2533016
vGLUT1	Abcam	ab77822; RRID:AB_2187677
Ki67	Agilent	M724029; AB_2687528
FITC-Ki67	Thermo Fisher	11-5698-82; RRID:AB_11151330
FACS control	Thermo Fisher	11-4321-80; RRID:AB_1834375
Chemicals, peptides, and recombinant proteins		
harmine	Sigma	286044
17-β-estradiol	Sigma	E8875
TG003	Sigma	T5575
cyclopamine	Fisher	S1146
proINDY	Ogawa et al., 2010	N/A
SAG	Sigma	SML1314
moclobemide	Sigma	M3071
aromatase inhibitor I	EMD Millipore	182540
NCI Approved Oncology Drug Set VIII	National Cancer Institute	https://dtp.cancer.gov/organization/dscsb/obtaining/available_plates.htm
Deposited data		
<i>Xenopus</i> drug treatment brain RNA-Seq	GEO	GSE155554
<i>Xenopus</i> brain RNA-Seq time course	GEO	GSE155554
Human primary cells microarray data	GEO	GSE155552
Human NPC <i>ESR2</i> CRISPRi transcriptomics	GEO	GSE155552
Experimental models: cell lines		
WTC11	Mandegar et al., 2016	N/A
eWT-1323.4	Matsumoto et al., 2013	N/A
28126	Gallego Romero et al., 2015	N/A
Experimental models: organisms/strains		
<i>Xenopus tropicalis</i>	National <i>Xenopus</i> Resource (RRID: SCR_013731)	Superman strain
<i>Xenopus tropicalis</i>	Khokha Lab (Yale)	Superman strain
<i>Xenopus tropicalis</i>	Nasco, Fort Atkinson, WI	LM00822
Oligonucleotides		
<i>dyrk1a</i>	Gene Tools; Blackburn et al., 2019	5'-TGCATCGTCTCTTTCAAGTCTCAT-3'
<i>ERβ/esr2</i>	Gene Tools	5'-GTGCATGTAAGTGGACATTTTTAAC-3'
<i>aromatase/cyp19a1</i>	Gene Tools	5'-GGGATTCAAGGCTCCATAATCACG-3'
Recombinant DNA		
CMV:hDYRK1A-GFP	Willsey et al., 2020	N/A
Software and algorithms		
Fiji / ImageJ	https://fiji.sc	v2.0.0
GraphPad Prism	https://www.graphpad.com	v8.3
Scripts and data used in analyses	This paper	https://bitbucket.org/willseylab/

RESOURCE AVAILABILITY

Lead contact

Further information and requests for resources and reagents should be directed to and will be fulfilled by the Lead Contact, Matthew State (matthew.state@ucsf.edu).

Materials availability

- Plasmids generated in this study are available upon request.

Data and code availability

- All code used for RNA-seq data processing and associated transcriptional analyses, as well as post-processed expression data (e.g., raw counts, normalized counts), are under version control in BitBucket (<https://bitbucket.org/willseylab/>).
- Transcriptomics data discussed in this publication have been deposited in NCBI's Gene Expression Omnibus (Edgar et al., 2002) and are accessible through GEO Series accession number GSE155554 (*Xenopus* data) or GSE155552 (human data).

EXPERIMENTAL MODEL AND SUBJECT DETAILS

Animal models

Xenopus tropicalis adult breeding animals originated in the Khokha lab (Yale, wild-type *Superman* strain), in the National *Xenopus* Resource (RRID:SCR_013731, (Pearl et al., 2012), wild-type *Superman* strain) or from Nasco (Fort Atkinson, WI, wild-type). Animals were maintained in a recirculating system and used in accordance with approved UCSF IACUC protocols. Embryo stages 1–46 (Nieuwkoop and Faber, 1994) were used, as indicated in the manuscript. Males and females were used and clutch mates were always used as controls.

Cell lines

Cell lines WTC11 (male) (Mandegar et al., 2016), eWT-1323.4 (female) (Matsumoto et al., 2013), and 28126 (male) (Gallego Romero et al., 2015) were grown at 37°C in culture conditions indicated by cell line below.

METHOD DETAILS

Obtaining *Xenopus tropicalis* embryos and tadpoles

Induction of ovulation was achieved by injection of human chorionic gonadotropin (Sigma) into the dorsal lymph sac according to standard procedure (Sive et al., 2000) and in accordance with approved UCSF IACUC protocols. Natural matings and *in vitro* fertilizations were performed. Embryos and tadpoles were staged by Nieuwkoop and Faber (1994). Clutch mates were always used as controls.

Xenopus whole mount RNA *in situ* hybridization

A full probe plasmids list is presented in Table S1. Briefly, *Xenopus tropicalis* coding sequences for generating antisense probe were obtained from the IMAGE clone library (Morin et al., 2006) or TOPO cloned from *X. tropicalis* cDNA (iScript Reverse Transcription Supermix, BioRad, and TOPO II dual promoter kit, Fisher). The following were received as kind gifts: *ngn1-3* (Nieber et al., 2009) and *ptch1* (Koebernick et al., 2001). 11-UTP-Digoxigenin-labeled antisense probes were generated and whole-mount RNA *in situ* hybridization was conducted according to standard procedures with an anti-DIG AP antibody (1:3000, Sigma) and BM Purple (Sigma) (Harland, 1991). These stainings were done in a high-throughput basket format to accommodate many samples in parallel, using 100 μ m mesh (Sive et al., 2007) and 3D-printed racks (3D printer files are available at <https://willseyfroggers.org/home/resources/>). Embryos were imaged on a Zeiss AxioZoom.V16 with a 1X objective and extended depth of focus.

Xenopus brain time-course transcriptomics

Individual brains from untreated tadpoles stages 40–47 were dissected and immediately put in 200 μ l of cold Trizol (Thermo Fisher), pipetted with a fine needle to dissociate, and frozen at -80°C . 3 brains were pooled and 3 samples per condition were processed. RNA extraction, polyA selection, and low-input library preparation (500 bp size selection) were performed by the Functional Genomics Laboratory (UC Berkeley). Samples were processed together, barcoded, and spread across a sequencing lane to reduce batch effects. 150 base pair paired end sequencing was performed on an Illumina HiSeq 4000 by the Genomics Sequencing Laboratory (UC Berkeley).

RNA-Seq reads were aligned to the *X. tropicalis* v9.1 reference genome using STAR v2.7.3 (Dobin et al., 2013) in gene annotation mode. RNA-Seq quality control metrics were generated using Picard (v 2.21.1). Genes with greater than one count per million in at

least three samples were retained and full quantile normalization was performed across samples. *X. tropicalis* tadpole brain time course RNA-Seq data can be queried at <https://willseyfroggers.org/home/resources/>.

To compare the *Xenopus* developmental trajectory to human brain development, we performed a principal component analysis (PCA) of the BrainSpan human brain developmental transcriptome dataset ((Kang et al., 2011), <https://www.brainspan.org/static/download.html>) and then projected the *Xenopus* samples to PCA coordinate space. We used both the exon microarray and RNA-Seq (Gencode v10) datasets, summarized to gene level in order to confirm our results were not platform-dependent. The BrainSpan RNA-Seq dataset was subset to expressed genes defined as those having greater than three RPKM in at least five samples. Next, all gene expression datasets were reduced to a common gene set between the *Xenopus* dataset and human datasets (9,986 genes in BrainSpan RNA-Seq and 10,675 genes in BrainSpan exon array). In the *Xenopus* dataset, human gene orthologs in *Xenopus* which had multiple transcripts were collapsed and the median value across the three replicates was retained. Finally, the BrainSpan microarray data is summarized as $\log_2(\text{intensity})$ and therefore, we transformed both the *Xenopus* and the BrainSpan RNA-Seq datasets into $\log_2(\text{RPKM})$.

The BrainSpan data was zero centered and scaled prior to computing the principal components, and the *Xenopus* data were similarly centered and scaled prior to projection onto the PCs. Similar to findings reported in Kang et al. (2011), we observe that time appears to be the predominant contributor to variation in gene expression (PC1 orders by developmental stage). We then calculated an equivalent vector representing the scaled and centered *Xenopus* time course data and projected it onto the BrainSpan PCA coordinate space using the center point and rotations. In both BrainSpan datasets, the *Xenopus* time course samples trend in order from Stage 40-47 along PC1, suggesting a clear pattern of maturation, and developmentally span early mid prenatal to late prenatal human brain development (Figures S1C and S1D). For visual simplicity, we plot PC1 of both the RNA-Seq and exon array data, shown as bands of the 95% confidence interval of the mean for each major developmental stage, and then overlay the *Xenopus* sample projections along that trajectory in Figure 1B.

To approach this question with a different method, we leveraged Specific Expression Analysis (SEA) across brain regions and development (<http://genetics.wustl.edu/jdlab/csea-tool-2/>) (Xu et al., 2014). This tool takes as input a set of gene symbols and performs an enrichment analysis of gene expression across six brain regions and ten developmental stages as defined by BrainSpan. Each gene is given a Specificity Index threshold (pSI) which represent the gene's specificity for the given spatiotemporal window as specified. For each *Xenopus* stage we calculate the top 10% of expressed genes with a human gene ortholog and input this to SEA. Like the PCA above, we see a significant enrichment (BH adjusted p value < 0.05) for early fetal to early midfetal at stage 40, to late fetal at stages 45-47 across five brain regions. We again observe 'aging' as the *Xenopus* stages increase, providing evidence the analysis is sensitive enough to show gradual trends. For visual clarity and phenotypic relevance, we show the cortex specific values in Figure S1E and provide all p values for all regions in Table S2.

***Xenopus tropicalis* microinjections**

Xenopus tropicalis embryonic microinjections were performed as in Sive et al. (2000). Microinjections were performed at the 2-cell stage using a Narishige micromanipulator, Parker Picospritzer, and Zeiss Stemi microscopes. Injection volume was calibrated with an eye-piece micrometer. Embryos were grown between 22-25°C in 1/9 Modified Ringer's (MR) solution, which was refreshed daily. Male and female embryos were analyzed. See following sections and Table S1 for CRISPR injection details. The following morpholinos were used: *dyrk1a* (translation-blocking, 4 ng, 5'-TGCATCGTCTCTTTCAAGTCTCAT-3' (Blackburn et al., 2019)); *ERβ/esr2* (translation-blocking, 4 ng, 5'-GTGCATGTAAGTGGACATTTTAAAC-3'); *aromatase/cyp19a1* (translation-blocking, 4 ng, 5'-GGGATTC AAGGCTTCCATAATCACG-3').

***Xenopus* CRISPR/Cas9 genome editing**

Single guide RNAs (sgRNAs) were designed against the *X. tropicalis* genome version 9.1 with the CRISPRscan algorithm (Moreno-Mateos et al., 2015). sgRNAs were selected to have no predicted off-targets, to be high efficiency, and to target an exon as 5' within the gene as possible, as long as that exon was well conserved within vertebrates. A full list of sgRNA and genotyping sequences is presented in Table S1. sgRNAs were synthesized *in vitro* as in Bhattacharya et al. (2015) from DNA oligos (IDT DNA oligos, EnGen sgRNA synthesis kit) and purified (Zymo RNA clean & concentrator kit). For each embryo, 3 ng of purified Cas9-NLS protein (Macrolabs, UC Berkeley), 800 pg sgRNA, and a dextran dye conjugated with Alexa-555 (Invitrogen) were injected into 1 cell of a 2-cell stage embryo. The day following injection at stages 14-20, embryos were sorted left from right according to the dye.

***Xenopus* genotyping**

To select high-efficiency sgRNAs, we first injected the sgRNA, Cas9-NLS protein, and a fluorescent dextran tracer into both cells at the 2-cell stage. At tadpole stages, DNA was extracted from surviving animals. Briefly, tadpoles were incubated in 1X thermopol buffer (NEB) with 2 mg/ml proteinase K for 1 hour at 55°C, followed by 10 minutes at 95°C. 2 μl of the resulting supernatant was used as template for a standard genotyping polymerase chain reaction (PCR) reaction. PCR primers were designed such that the resulting amplicon would include 200 bp upstream of the PAM site and 300 bp downstream. A full list of primer sequences is presented in Table S1.

PCR products were Sanger sequenced with the forward primer (GeneWiz) and traces were deconvolved with TIDE (Tracking of INDEIs) software (Brinkman et al., 2014), a tool used to estimate sgRNA efficiency in *Xenopus* and zebrafish (Etard et al., 2017; DeLay

et al., 2018) since this mutagenesis approach largely generates insertion/deletion (INDEL) mutations (Moreno-Mateos et al., 2015). We tested at least two sgRNAs per gene and selected the sgRNAs with the highest mean efficiency, with the intention of creating severe loss of function mutations to be able to identify clear phenotypes (Figure S1; Table S1). These are likely conservative estimations of mutational efficiencies since this assay only quantifies INDEL mutations, and we only assayed animals that survived to tadpole stages as bilateral mutants.

Xenopus whole mount immunofluorescence

Tadpoles were fixed in 4% paraformaldehyde, bleached, and stained whole-mount according to (Willsey et al., 2018b). These stainings were done in a high-throughput basket format to accommodate many samples in parallel (Sive et al., 2007), but with a coarser mesh (200 μ m) and 3D-printed racks (3D printer files are available at <https://willseyfroggers.org/home/resources/>). Primary antibodies used were against β -Tubulin (DSHB, E7, 1:100); PCNA (PC10, Life Technologies, 1:50); vGLUT1 (Abcam, ab77822, 1:100).

Xenopus microscopy

All *Xenopus* images were acquired on a Zeiss Axio Zoom.V16 microscope with apotome and a 1X or 2.25X objective. For fluorescence images, a Zeiss 506 monochrome camera was used, and for color images, a Zeiss 105 or 712 color camera was used. A tadpole stamp was 3D-printed and used to make agarose molds to hold tadpoles during imaging, similar to that from Truchado-Garcia et al. (2018) (3D printer files are available at <https://willseyfroggers.org/home/resources/>). Images were processed using Fiji (Schindelin et al., 2012).

Xenopus brain size measurements

Brain region size was calculated from stereoscope images of brain immunostainings using the freehand select and measure functions in Fiji (Schindelin et al., 2012). For mutants, the injected side was compared to the uninjected side (internal control). Because there is no clear morphological demarcation separating the diencephalon and mesencephalon, they were measured together to increase the reproducibility of the measurement. These measurements were from two-dimensional images taken from a dorsal perspective and are a reflection of relative size differences, not a direct quantification of cell number. We have previously shown that this staining and imaging strategy recapitulates conclusions made from fixed sections, as our staining penetrates the entire brain and our imaging is projections of optical sections (Willsey et al., 2018b). Higher resolution imaging and quantification is technically achievable, but not feasible here due to the number of animals required for each assay (Figure S2).

CRISPRi experiments in human NPCs

Neural progenitor cells (NPCs) were generated from a derivative of the male WTC11 iPSC line that has been genetically engineered to contain a constitutively expressed dead Cas9 (dCas9) fused to the transcriptional repressor domain 'KRAB' (dCas9-KRAB) (Mandegar et al., 2016). NPCs were generated by dual SMAD inhibition and Wnt signaling inhibition of iPSCs using an adapted small molecule protocol (Qi et al., 2017). Specifically, cells were treated with LDN193189, SB431542, and XAV939 for 6 days, were passaged, and then treated with only XAV939 for an additional 2 days to obtain NPCs. NPCs were maintained on Matrigel (Corning) coated tissue culture plates in neural progenitor medium (NPM) (DMEM/F12, 1x N2, 1x B27 -Vitamin A, 1x GlutaMAX, 1x MEM-NEAA, 10 ng/ml FGF2, 10 ng/ml EGF).

sgRNAs were designed using "CRISPRiDesign" and cloned into the PLG15 lentiviral vector for expression from a mouse U6 promoter (Horlbeck et al., 2016). The sgRNA sequences are: *DYRK1A* (5'-AGAGCGGACACCCCGAGCGG-3'); *NRXN1 α* (5'-GACTGCTGCTGCCTTTTCAG-3'); *ADNP* (5'-GGTGGGAGAGGCGGCTTCAC-3'); *CHD2* (5'-GGCAGAGCGCGCTCTCTCTA-3'); *POGZ* (5'-GCGCTCGGCGAGGCGTTCAG-3'); non-targeting sgRNA #1 (5'-GCAGGCCCGTTTGCTTACGA-3'); and non-targeting sgRNA #2 (5'-GTCCACCCCTTATCTAGGCTA-3'). Lentivirus was produced by transfecting Lenti-X 293T with standard packaging vectors using *Lipofectamine 2000* Transfection Reagent (Invitrogen). Viral supernatant was harvested 72 hours following transfection and filtered through a 0.45 μ m PVDF syringe filter. Filtered virus was using Lenti-X concentrator (Takara Bio) and HEK293 media was replaced with NPM media. To construct the CRISPRi cell lines, WTC11 dCas9 NPCs were lentivirally transduced. The sgRNA was expressed using a lentiviral U6 based expression vector derived from pSico that co-expresses BFP (Chen et al., 2013). We performed quantitative PCR to validate gene repression efficiency.

Human CRISPRi NPC proportion quantification

To quantify the proportion of proliferative NPCs in our CRISPRi lines, we first dissociated the cultures into single cells using Accutase (StemCell Technologies, Inc.). We performed one-step intracellular staining for proliferation marker Ki67 using eBioscience Foxp3 / Transcription Factor Staining Buffer Set (Thermo Fisher Scientific) as described in the product manual. We utilized the FITC-conjugated anti-Ki67 primary antibody (Thermo Fisher Scientific; Catalog # 11-5698-82) and its isotype control antibody (Thermo Fisher Scientific; Catalog # 11-4321-80) at 1:1000 dilution. We ran flow cytometry on BD FACSCanto II to quantify the percentage of Ki67-positive cells in each sample. We normalized each sample to its paired non-targeting sgRNA control line.

PCNet hcASD gene interconnectivity analysis

We downloaded PCNet-V1.3 (Huang et al., 2018) via the Cytoscape v3.8.1 NDEX browser (also available at <https://www.ndexbio.org/#/network/4de852d9-9908-11e9-bcaf-0ac135e8bacf>). We then exported from Cytoscape the PCNet-V1.3 Edge Table (*Updated_PCNetv1.3_default_edge.csv*), and extracted interactions to a 2-column format (*generate_PCNet-V1.3_interactions.sh*).

To assess interconnectivity of hcASD genes in PCNet (Figure 3B), we calculated 3 measures of interconnectivity: (A) total number of pairwise connections between hcASD genes, (B) total number of hcASD genes connected to another hcASD gene (e.g unique genes from A), and (C) number of direct connections between hcASD genes and any other PCNet genes. To determine the significance of these observations, we performed permutation testing. We permuted hcASD genes by randomly selecting sets of 102 genes from all autosomal genes characterized in Satterstrom et al. (2020) (the majority of these genes are not significantly associated with ASD); we weighted gene sampling probability by total gene mutability, calculated by summing the individual probabilities for protein-truncating variants, missense A variants, and missense B variants from Satterstrom et al. (2020). We generated 1,000 sets of permuted hcASD genes (*permute-hcASD-genes.R*), and calculated the 3 measures of connectivity described above. We then estimated the significance of the observed measures of hcASD gene interconnectivity based on the number of times out of 1,000 that we observed a permuted value \geq the observed value (*permutationTest_PCnet-connectivity.R*).

Constructing hcASD networks

We defined hcASD genes as the 102 ASD genes for which FDR < 0.01 in Satterstrom et al. (2020). To construct the hcASD network, we identified all PCNet interactions for which at least one gene in the interaction was an hcASD risk gene. We defined nodes of the hcASD network to be all hcASD genes and their direct interactors. We subsequently used PCNet interaction data to fill in edges between these nodes (*parse_PCNet.R*, *Satterstrom_2020_TADA_asd.xlsx*).

BrainSpan layer-specific data

We obtained region- and layer-specific gene expression data from the BrainSpan Prenatal LMD Microarray Dataset (Miller et al., 2014). The data can be downloaded directly from BrainSpan at <http://www.brainspan.org/static/download.html>. This dataset profiles gene expression in four brains spanning 15–21 post-conception weeks. In each brain, gene expression profiles were assessed for hundreds of laser microdissected tissue samples from subdivisions distributed across cortical and non-cortical regions. For more information on data generation, please see the corresponding technical white paper on the project website (<http://www.brainspan.org/>).

We trimmed the BrainSpan expression data to samples from PCW15 and PCW16 donors and utilized expression data corresponding to frontal neocortex only (as done in Willsey et al., 2013). Within the frontal neocortex, we assessed samples from 7 of the 9 layers: outer cortical plate, inner cortical plate, subplate zone, intermediate zone, outer subventricular zone, inner subventricular zone, and ventricular zone (listed from cortical to ventricular surface). We excluded subpial granular zone and marginal zone layers due to insufficient sample numbers (< 5). For each layer, we collapsed expression data from probe- to gene-level by removing probes not detected above background (DABG) in one or more samples, then calculating the median expression, per gene, of remaining probes within each sample. We also removed genes that were not represented in PCNet (*parse_layer-specific-data.R*).

PCNet average gene connectivity

To determine whether PCNet identifies molecular interactions that tend to correspond to higher gene expression correlations within BrainSpan data, we calculated Spearman's correlations for all gene-gene pairings for genes that were both expressed in the layer and represented in PCNet. We grouped these gene-gene interactions into 1) within PCNet, or 2) not within PCNet, and calculated the average of gene-gene interaction for each group. We subsequently performed a paired t test (paired by layer) to determine whether there was a difference in average gene-gene correlation for interactions in PCNet versus interactions not in PCNet (Figure 4C) (*parseBrainspan_pcw15-16.R*, *Pcnet_avgGeneCor.R*, *Satterstrom_2020_TADA_asd.xlsx*).

BrainSpan layer-specific hcASD network connectivity analysis

To assess the relevance of the hcASD network to each of the seven fetal layers, we recreated the hcASD network within each layer (based on expression data from samples collected within that layer only) and then assessed its connectivity. Specifically, we trimmed the interaction network to expressed genes only and then determined Spearman's correlation coefficients between connected hcASD network genes, using expression data from each layer separately. By summing the absolute values of these correlations, we were able to estimate the overall connectivity of the networks layer-by-layer. We calculated normed correlations in order to remove biases that have to do with global changes in connectivity.

Let i and j denote genes and k denote layer. Define r_{ijk} as the Spearman's correlation between genes i and j in layer k , and define r_k as the average correlation, over all pairs of the genes measured in layer k . Then define a normed correlation as: $c_{ijk} = \left(r_{ijk} / r_k \right)$. We then calculated normalized connectivity of a network in layer k by summing the absolute value of c_{ijk} for all pairs in the network, and calculated average hcASD risk gene network connectivity (Figures 3D and 3E) by dividing layer connectivity by the number of edges in the hcASD network.

We assessed the significance of these observed layer-specific connectivities by permuting layer-specific correlations. We conducted permutation testing separately for each layer, as individual layers have slightly different hcASD networks based on differences in gene expression. Within each layer, for each connected hcASD network gene pair, we calculated the normalized Spearman's correlation coefficient from a randomly selected layer. If this could not be calculated from the sampled layer (e.g., one of the genes is not expressed), we continued sampling until the gene pair is recovered. We normalized the randomly sampled correlation value based on the average correlation (r_k) for the randomly sampled layer. We then calculated the permuted connectivity by summing the sampled correlations for every gene pair, and average permuted hcASD gene network connectivity by dividing by the number of edges in the interaction network. We conducted 10,000 permutations for SP, SVZI and CPi; and 1,000 permutations for the rest of the layers (as $p = 1$ after 1,000 iterations for these layers). We estimated the significance of the observed connectivity based on the number of times we observed a permuted value \geq the observed value (Figures 4D and 4E) (*connectivity_byLayer.R*, *makePermutationTestPlots.R*).

All code used for PCNet and BrainSpan data processing and associated connectivity analyses, as well as post-processed interaction and expression data, are under version control in BitBucket (<https://bitbucket.org/willseylab/>), and will be made publicly available on the date of publication.

Xenopus small molecule treatments

Small molecules used were: harmine (Sigma 286044, 0.6–1.5 μ M); TG003 (Sigma T5575, 10 μ M); 17- β -estradiol (Sigma E8875, 5–20 μ M); cyclopamine (Fisher S1146, 2.5–10 μ M); proINDY (5 μ M; (Ogawa et al., 2010)); SAG (Sigma SML1314, 5 μ M); moclobemide (Sigma M3071, 10 μ M); aromatase inhibitor I (EMD Millipore 182540, 50 μ M). Small molecules were resuspended as 10 mM solutions in DMSO. For treatment, solutions were diluted in 1/9 MR solution. DMSO controls were DMSO added at the same volume as the small molecule in 1/9 MR. Moclobemide (a monoamine oxidase inhibitor) was used as a control for harmine since its predicted off-target is monoamine oxidase (Lieberman et al., 1994). Animals were treated in 5 mL solutions in 6-well culture plates with small molecules at stage 30 at given concentrations unless otherwise indicated. Drug solutions were not refreshed. Any dead animals were removed as soon as they were found. Animals were grown between 22–24°C and always alongside their DMSO control. See key reagents above for small molecule product information. The NCI Approved Oncology Drug Set VIII was received from the National Cancer Institute of the National Institutes of Health (https://ntp.cancer.gov/organization/dscb/obtaining/available_plates.htm) and all compounds were tested at 10 μ M in combination with 1.25 μ M harmine.

Xenopus drug treatment transcriptomics

For drug treatment transcriptomics, individual brains from stage 46 tadpoles treated with DMSO, 10 μ M 17- β -estradiol, or 5 μ M cyclopamine starting at stage 30 were dissected and immediately put in 200 μ l of cold Trizol (Thermo Fisher), pipetted with a fine needle to dissociate, and frozen at -80°C . 3 brains were pooled and 3 samples per condition were processed. RNA extraction, polyA selection, and low-input library preparation (500 bp size selection) were performed by the Functional Genomics Laboratory (UC Berkeley). Samples were processed and barcoded together, then spread across sequencing lanes together to reduce batch effects. 150 base pair paired end sequencing was performed on an Illumina HiSeq 4000 by the Genomics Sequencing Laboratory (UC Berkeley).

RNA-Seq reads were aligned to the XenBase *X. tropicalis* v9.1 reference genome using STAR v2.7.3 (Dobin et al., 2013) in gene annotation mode. Alignment, RNA-Seq, and hybrid-selection quality control metrics were generated using Picard (v 2.21.1). Principal component analysis (PCA) of the quality control matrices did not indicate any sample outliers. Genes with more than 1 count per million in at least three samples were retained for clustering and differential gene expression (DEX) analysis. To determine any sample outliers by gene expression, we performed complete-linkage clustering based on the Euclidean distance of the Pearson correlation matrix. We defined an outlier as a sample which only shared the deepest node with replicates. No outliers were detected. Filtered genes were tested for differential expression using DESeq2 v1.24.0 (Love et al., 2014) with shrinkage estimator apeglm (Zhu et al., 2019). Significantly DEX genes were genes that pass a 0.05 significant threshold. Gene Ontology enrichment analysis of annotated DEX genes was performed using the PANTHER online classification tool (Mi et al., 2010) using all expressed genes as a background ($N = 10784$) and the GO-Slim annotation Table Sets for *Xenopus tropicalis*. Restricting our DEX lists to genes with an absolute log₂ fold change greater than 1, there were 320 DEX genes when comparing 17- β -estradiol to DMSO treatment, 1112 DEX genes when comparing cyclopamine to DMSO treatment, and 235 genes occurred in the same direction in both lists. We used a one-tailed hypergeometric test to the likelihood of enrichment between DEX lists over all expressed genes and determined the overlap was significant ($p = 8.83\text{e-}213$).

Human CRISPRi NPC estrogen treatment

We reconstituted 17- β -estradiol in DMSO. We seeded NT-sgRNA and ASD gene-sgRNA NPCs generated as described above on Matrigel coated wells of 12 well plates and treated the cells with DMSO or 5 μ M 17- β -estradiol for 5 days. We included 3 wells per treatment per cell line. We refreshed DMSO or 17- β -estradiol containing NPM daily for 5 days and then quantified Ki67+ proportion by FACS as described above. Samples were normalized to paired non-targeting control lines. Since NPC proportion following *POGZ* repression was not significantly different (Figure 3E), we did not carry it forward for testing with estrogen. In testing *CHD2* repression, the plate became confluent before we were able to quantify, and therefore the experiment was excluded. Differences in effect size compared to the experiments in Figure 3 are likely due to differences in confluency, since cells were grown 2 days longer for drug treatment.

Organoid generation and drug treatment

Cerebral organoids were generated based on a previously published method (Paşca et al., 2015) with several modifications. Briefly, hiPSCs cultured on Matrigel were dissociated into clumps using 0.5 mM EDTA in $\text{Ca}^{2+}/\text{Mg}^{2+}$ -free DPBS and transferred into ultra-low attachment 6-well plates in neural induction media (GMEM containing 20% (v/v) KSR, 1% (v/v) penicillin-streptomycin, 1% (v/v) non-essential amino acids, 1% (v/v) sodium pyruvate, and 0.1 mM 2-mercaptoethanol). For the first nine days, neural induction media was supplemented with the SMAD inhibitors SB431542 (5 μM) and dorsomorphin (2 μM) and the Wnt inhibitor IWR1- ϵ (3 μM), with a media exchange performed every three days. Additionally, the Rho Kinase Inhibitor Y-27632 (20 μM) was added during the first six days of neural induction to promote survival. Between days 9–25, organoids were transferred to a neural differentiation media (1:1 mixture of Neurobasal and DMEM/F12 containing 2% (v/v) B27 without vitamin A, 1% N2, 1% (v/v) non-essential amino acids, 1% (v/v) Glutamax, 1% (v/v) antibiotic/antimycotic, 0.1 mM 2-mercaptoethanol) supplemented with FGF2 (10 ng/mL) and EGF (10 ng/mL). Between days 25–35, organoids were maintained in neural differentiation media without FGF or EGF. From Day 35 onward, organoids were maintained on a shaker in neural differentiation media containing B27 with vitamin A with media exchanges three times per week.

For the drug treatments, two organoids per condition were placed in each well of a 24-well plate and treated with DMSO, 20 μM 17- β -estradiol, 2 μM harmine, or the combination of both drugs for seven days. Media changes were performed every two days with addition of fresh drugs. After seven days, organoids were fixed in 4% PFA for 1 hour, washed three times with PBS for 10 minutes, incubated in 30% sucrose overnight, and frozen in OCT/30% sucrose 50/50 (v/v) for further cryosectioning.

Organoid staining & imaging

Frozen organoids underwent cryosectioning into 14 μm sections (CryoStar NX50), with 8–10 serial sections made from each organoid. For immunostaining, first the sucrose/OCT media was washed away by a brief wash in PBS. Antigen retrieval was done by a 15-minute wash in boiling 10 mM Sodium Citrate (pH = 6) solution. Blocking was a 1-hour wash in donkey blocking buffer (DBB: 10% donkey serum and 1% triton-X in PBS) in a humidified slide box. Primary mouse Ki67 antibody (Dako, MIB1 clone, M7240) was diluted 1:200 in DBB + 1% Triton X-100 and subsequently added to each slide. The samples were incubated in a humidified slide box at 4°C overnight. The next day, the slides were washed 3 times for 20 minutes each with PBSTx (PBS + 0.1% triton-X). In the humidified slide box, samples were incubated in secondary antibody (anti-mouse IgG conjugated to Alexa546, 1:1000 in DBB + 1% triton-X) at room temperature for 2 hours. After washes in PBSTx for 1 hour, 200 μL of DAPI Fluoromount-G (SouthBiotech) was added before coverslipping. The slides were dried at room temperature and sealed with nail polish.

Sections were imaged on a Leica SP8 confocal with 40X objective. Images were processed using FIJI/ImageJ (NIH) and compiled in Illustrator (Adobe). Number of Ki67+ and DAPI+ cells in each image were acquired in FIJI using standardized thresholding and the 'analyze particles' function. At least two independent lines and organoids were quantified for each condition, with representative images presented.

Human PCW6-10 transcriptome analysis & comparison to *Xenopus*

Raw microarray data from Csöregi et al. (2009) was downloaded from GSE17645 and GSE10097. This included two Table Sets, the first comparing primary PCW6-10 neuron culture with and without 2 μM 17- β -estradiol treatment for 7 days and the other doing the same for PCW6-10 neuron plus glia culture. In both cases, cells originated in dorsal and ventral regions of the developing brain. The GCRMA package v2.56.0 was used to read the CEL files, adjust for optical noise and non-specific binding, and finally perform quantile normalization. Quality of the microarray was evaluated pre- and post-normalization using the arrayQualityMetrics package v3.40.0 and identified no outlying samples. Probes with a maximum normalized expression value less than 4 were removed for low representation. Genes with multiple probes were collapsed and the median value of the probe set group was retained. Differential expression analysis was performed with the limma package v3.40.6 comparing the two estradiol treatments against the two primary cultures. Given the high intra-group variability across the neuron culture and neuron plus glia culture, we expect to detect genes with strong transcriptional changes in both conditions but do not expect them to necessarily reach statistical significance, which is what we ultimately see. Of the 7,109 final genes tested in the microarray, 6,231 were found to have homology with genes in *Xenopus tropicalis*, recovering 536/1461 DEX genes identified in the estrogen treatment in *Xenopus*. Of the 536 *Xenopus* DEX genes, 82 also showed a strong transcriptional response in human primary tissue, 68 of which were in the same direction.

All code used for RNA-Seq data processing and associated transcriptional analyses, as well as post-processed expression data (e.g., raw counts, normalized counts), are under version control in BitBucket (<https://bitbucket.org/willseylab/>), and will be made publicly available on the date of publication.

ESR2 CRISPRi in NPCs

A human CRISPRi NPC line for *ESR2* was generated as above with sgRNA (5'-GCGAGCTGCGACGGGCTCTG-3') and compared to a non-targeting control sgRNA (NT-sgRNA) (5'-GTCCACCCTTATCTAGGCTA-3'). NPCs were grown in NPM media (50% DMEM F12, 50% Neurobasal media, 1x Glutamax, 0.5x N2, 0.5x B27 minus vitamin A, 20 ng/mL basic FGF). We measured *ESR2* transcript expression and validated sgRNA repression efficiency by quantitative PCR (qPCR) (Figure S5). We extracted total RNA from NPCs with non-targeting sgRNA and NPCs with *ESR2* sgRNA using Rneasy Mini kit (QIAGEN). Then we converted the total RNA into cDNA using a High Capacity cDNA Reverse Transcription Kit (Thermo Fisher Scientific) according to the manufacturer protocol. We performed qPCR using PowerUp SYBR Green Master Mix on QuantStudio 6 Flex Real-time PCR machine (Thermo Fisher

Scientific). The primers used for *ESR2* were 5'-GATCGCTAGAACACACCTTACC-3' and 5'-AGTGAGCATCCCTCTTTGAAC-3'. The fold change of *ESR2* in the *ESR2* CRISPRi NPCs was calculated by comparative Ct.

ESR2 and NT-sgRNA CRISPRi NPCs were differentiated for 6 days on Matrigel in neuronal differentiation medium (DMEM/F12, 1x N2, 1x B27 -Vitamin A, 1x GlutaMAX, 1x MEM-NEAA, 0.5 mM dibutyryl cAMP, 0.2 mM ascorbic acid, 1 μ M PD0325901, 5 μ M SU5402, 10 μ M DAPT, 20 ng/mL BDNF) with media changes every other day. Cells were harvested for RNA extraction and cDNA synthesis at differentiation days 0 and 6. We used cDNA converted from 10 ng total RNA for each sample to generate libraries with the Ion Ampliseq Transcriptome Human Gene Expression Chef-Ready Kit (Life Technologies) according to the recommended protocol. The resulting libraries were templated onto Ion 540 Chips using the Ion Chef system and sequenced on the Ion GeneStudio S5 System.

ESR2 CRISPRi transcriptomic analysis

Raw data was processed with the Ion Torrent Suite Server v5.8.0 (ThermoFisher). Reads were aligned to the hg19 AmpliSeq Transcriptome reference (v1.1) with the coverageAnalysis plugin v5.8.0.8. This plugin also generated quality information. Reads were quantified using the ampliSeqRNA plugin v5.8.0.3 with default settings. Genes with greater than 1 count per million in three samples were retained for clustering and DEX analysis. No outlier samples were determined. Genes were tested for differential expression using DESeq2 v1.24.0 (Love et al., 2014) with shrinkage estimator apeglm (Zhu et al., 2019). Significantly DEX genes are genes that pass a 0.05 significance threshold.

QUANTIFICATION AND STATISTICAL ANALYSIS

GraphPad Prism software version 8.3 was used to graph data and determine statistical significance for all *Xenopus* and organoid experiments. Changes in variance were tested by a Brown-Forsythe test. Mean comparisons were tested for statistical significance using a nonparametric Mann-Whitney rank-sum test. For all tests, p values less than 0.05 were considered significant. The effects of CRISPR-induced mutations are likely underestimated considering animals were not genotyped before phenotyping, due to the necessarily high-throughput nature of this work. Therefore, many animals are likely not mutant or are mosaic and penalize the statistical tests.

ADDITIONAL RESOURCES

3D printer files and *Xenopus* time course brain transcriptomic data can be accessed at: <https://willseyfroggers.org/home/resources/>.